Research Viewpoint on Performance Enhancement for Very-High-Cycle Fatigue of Ti-6Al-4V Alloys via Laser-Based Powder Bed Fusion

Gao, Chun; Zhang, Yang; Jiang, Jingjiang; Fu, Rui; Du, Leiming; Pan, Xiangnan

DOI
10.3390/cryst14090749

Publication date
2024

Document Version
Final published version

Published in
Crystals

crystals

MDPI

Review

Research Viewpoint on Performance Enhancement for Very-High-Cycle Fatigue of Ti-6Al-4V Alloys via Laser-Based Powder Bed Fusion

Chun Gao [1,2], Yang Zhang [3], Jingjiang Jiang [4], Rui Fu [5], Leiming Du [6] and Xiangnan Pan [7,*]

1 School of Civil Engineering, Harbin University, Harbin 150086, China; gaochun@hrbu.edu.cn
2 Heilongjiang Province Key Laboratory of Underground Engineering Technology, Harbin University, Harbin 150086, China
3 China Construction Sixth Engineering Division Co., Ltd., Tianjin 300012, China; zhangyang39@cscec.com
4 College of Aerospace and Civil Engineering, Harbin Engineering University, Harbin 150001, China; jiangjingjiang@hrbeu.edu.cn
5 School of Mechanical Engineering, Guangxi University, Nanning 530004, China; furui@gxu.edu.cn
6 Department of Microelectronics, Delft University of Technology, 2628 CD Delft, The Netherlands; l.du@tudelft.nl
7 LNM, Institute of Mechanics, Chinese Academy of Sciences, Beijing 100190, China
* Correspondence: panxiangnan@lnm.imech.ac.cn

Abstract: Additive manufacturing (AM) or 3D printing is a promising industrial technology that enables rapid prototyping of complex configurations. Powder Bed Fusion (PBF) is one of the most popular AM techniques for metallic materials. Until today, only a few metals and alloys are available for AM, e.g., titanium alloys, the most common of which is Ti-6Al-4V. After optimization of PBF parameters, with or without post processing such as heat treatment or hot isostatic pressing, the printed titanium alloy can easily reach tensile strengths of over 1100 MPa due to the quick cooling of the AM process. However, attributed to the unique features of metallurgical defects and microstructure introduced by this AM process, their fatigue strength has been low, often less than 30% of the tensile strength, especially in very-high-cycle regimes, i.e., failure life beyond 10^7 cycles. Here, based on our group's research on the very-high-cycle fatigue (VHCF) of additively manufactured (AMed) Ti-6Al-4V alloys, we have refined the basic quantities of porosity, metallurgical defects, and the AMed microstructure, summarized the main factors limiting their VHCF strengths, and suggested possible ways to improve VHCF performance.

Keywords: titanium alloy; additive manufacturing (AM); powder bed fusion (PBF); heat treatment; hot isostatic pressing (HIP); very-high-cycle fatigue (VHCF); crack initiation; metallurgical defect; microstructure; fatigue strength

Citation: Gao, C.; Zhang, Y.; Jiang, J.; Fu, R.; Du, L.; Pan, X. Research Viewpoint on Performance Enhancement for Very-High-Cycle Fatigue of Ti-6Al-4V Alloys via Laser-Based Powder Bed Fusion. *Crystals* **2024**, *14*, 749. https://doi.org/10.3390/cryst14090749

Academic Editor: Umberto Prisco

Received: 31 July 2024
Revised: 14 August 2024
Accepted: 20 August 2024
Published: 23 August 2024

1. Introduction

Titanium (Ti) is known as the rising third metal element, after iron (Fe) and aluminum (Al), and titanium alloys are widely used in a variety of engineering and living scenarios. The element titanium has an isotropic transition: being α phase with hexagonal close-packed (HCP) lattice at temperatures below 882.5 °C, i.e., β transus, in standard atmosphere, and β phase with body-centered cubic (BCC) lattice at high temperatures above β transus. Some chemical elements, e.g., Al and vanadium (V), can alloy titanium alloys to stabilize their α and β phases, called α and β stabilizing elements, respectively. Depending on the content of α and β stabilizing elements, titanium alloys can be divided into four types: near α, α + β, metastable β, and β [1,2].

Additive manufacturing (AM), also known as 3D printing, is a form of rapid prototyping, a technique for constructing objects by printing layer by layer from a digital model file using bondable materials such as powdered metals or photosensible resins [3]. Powder

bed fusion (PBF) is one of the advanced AM technologies, which has gradually matured over a long period of research and industrial development [4–9]. This development has enabled the widespread adoption of commercial applications of PBF, particularly to produce high-value products that are not technically feasible with traditional manufacturing processes [10–14]. Figure 1a gives an illustration of PBF with a scan strategy of meandering paths [15]. At first, a powder bed of metallic materials was stacked layer by layer with a thickness of t, and then a moving heat source with a power of p, usually a laser or electron beam, was focused on the top of the powder bed along a specific track with a velocity of v. As the beam scanned, the powder melted, fused, and solidified at a rapid cooling rate; the interval between two adjacent scan tracks is called the hatch spacing of h. After completing the programmed path for the current layer of powder, a roller restacked the new powder on top of the current layer to form a new layer of powder, and the previous scanning operation was replicated, with the scan path typically requiring a rotation angle of θ. These steps would be repeated many times until the designed specimen was finally 3D printed.

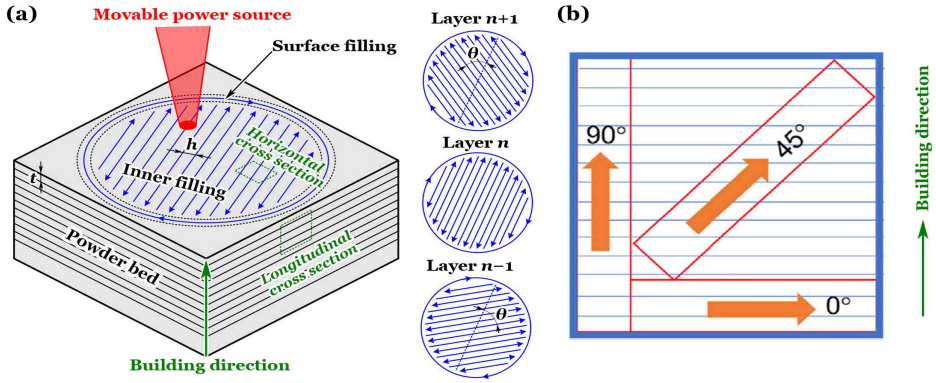

Figure 1. (**a**) Schematic drawing for powder bed fusion (PBF) with a scan strategy of meandering paths [15]. (**b**) The 3D printed specimens [16] with orientations of 0°, 45°, and 90°.

Figure 1b depicts an additively manufactured (AMed) titanium alloy of Ti-6Al-4V [16], which is an α + β type, via laser PBF technique (L-PBF) with different orientations of 0° (horizontally printed), 45°, and 90° (vertically printed). Ti-6Al-4V is the most used titanium alloy [1,2] and one of the few metallic materials suitable for AM [3,4]. Given the unique microstructure produced by the rapid cooling of the AM process, the AMed Ti-6Al-4V is very easy to make at the ultimate tensile strength (UTS) of $\sigma_u > 1100$ MPa, and can provide access to the category of so-called high-strength titanium alloys [17]. For the conventional melting–forging process, the manufactured high-strength titanium alloys have almost always been preferred to the use of a metastable β type [17].

Nevertheless, the AM process may also cause unavoidable metallurgical defects [18], e.g., lack-of-fusion (LoF), gas pores, keyholing pores, and other AM pores. These AM defects will greatly deteriorate the microstructural integrity of AMed materials and significantly reduce their fatigue strengths, particularly for the cases of loading number $N > 10^7$ cycles. It should be noted that fatigue strength is one of the most important mechanical properties of structural materials in real-world practical applications [19–21], as fatigue loading is ubiquitous and causes the vast majority of engineering failures, estimated at 4% GDP loss [22].

Figure 2 presents an example [23], in which a batch of pre-alloyed Ti-6Al-4V powder was used to vertically print axisymmetric specimens via L-PBF with ten combinations of processing parameters and a heat treatment of stress relief by heating at 600 °C for 2 h then cooling in a vacuum furnace. These combinations were named as Group 1, Group 2, . . ., Group 10. Figure 2a shows the tensile properties of the yield strength σ_y, the UTS σ_u, and the total elongation of ε_t at fracture under quasi-static monotonic loading; Figure 2b shows the fatigue strengths of σ_{w7} at 10^7 cycles, i.e., the traditional fatigue limit [24,25], and σ_{w8} at 10^8 cycles under axially ultrasonic cycling with resonant frequency of 20 k ± 500 Hz at

stress ratio of $R = -1$. In Figure 2, the abscissa $E = p/(t{\cdot}v{\cdot}h)$ is the volumetric energy density of the movable power source [26].

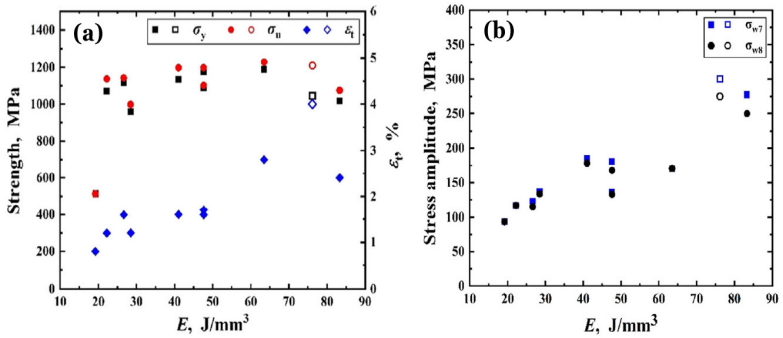

Figure 2. Tensile (**a**) and fatigue (**b**) properties of a titanium alloy with Groups 1~10 of processing parameters via laser powder bed fusion and experienced through annealing [23]. σ_y: yield strength, σ_u: ultimate tensile strength, ε_t: total elongation at fracture; σ_{w7}: fatigue strength at 10^7 cycles, σ_{w8}: fatigue strength at 10^8 cycles; solid symbols denoting Groups 1~9, and hollows denoting Group 10.

2. Aim and Objectives

Because of its importance in engineering, as mentioned above, metal fatigue [27,28] has been studied for a long time, dating back to the pioneering work of Wöhler [29] in the mid-19th century. According to conventional knowledge [19,24,27], there is a distinct fatigue limit for some metallic materials, such as ferrous alloys and titanium alloys. The fatigue limit is a level of stress amplitude σ_a or maximum stress σ_{max} below which an infinite number of loading cycles can be applied to a material without causing fatigue failure [19,24,25,27,28,30,31]. In engineering [32], the number of loading cycles is usually set at 10^7, and in this case, the fatigue limit is called the traditional fatigue limit [19,24,27].

Forty years ago, Atrens et al. [33] reported that fatigue failure still occurs after 10^7 cycles in a titanium alloy. This failure phenomenon has been named superlong [34,35] or ultralong [28] life fatigue, gigacycle fatigue [25,36], and ultra- [37] or very-high-cycle fatigue (VHCF) [38–40] successively. With the development of modern civilization, there is an urgent need for service components [41–43] that require a longer safe life, e.g., due to the high-frequency effects of flutter, many critical components in the aerospace industry can accumulate 10^7 cyclic loads every 3 h, including turbine engine fans and compressor blades. Therefore, the VHCF of titanium alloys, specifically Ti-6Al-4V, produced by conventional [39,43–45] and additive manufacturing [46–50], has attracted increasing attention in both scientific and industrial communities.

The authors and co-workers have systematically investigated the VHCF behavior of AMed Ti-6Al-4V and obtained extensive experimental results, which will be further discussed in-depth below. Based on these results, and with reference to the literature, this paper presents a research viewpoint to clarify the material characteristics, e.g., porosity, metallurgical defect types, and the microstructure of AMed Ti-6Al-4V, to summarize the main factors that will degrade the VHCF strengths, and to propose the applicable methods that will improve the VHCF performance.

3. Additively Manufactured Titanium Alloys

3.1. Porosities and Metallurgical Defect Types

Although the heat treatments of annealing types may degrade the tensile strength of AMed Ti-6Al-4V [49,50], the majority of the obtained UTS values in Figure 2a still satisfy $\sigma_u > 1100$ MPa. In contrast, the greatest of the fatigue strengths σ_{w7} and σ_{w8} does not exceed 300 MPa. Obviously, even if the applied stress amplitude σ_a is less than the traditional fatigue limit of σ_{w7}, the fatigue failure will occur during $N > 10^7$ cycles as long as $\sigma_a > \sigma_{w8}$. This falls into the scope of very-high-cycle fatigue (VHCF) [34–40].

In this regard, Du et al. [23] sequentially used the methods of Archimedean drainage and cross section to measure the porosity R_D of the AMed specimens for Groups 1~10. Figure 3 exhibits the distributed AM defects for Groups 1~9 on the selected representative regions within the horizontal and longitudinal cross sections cut from their specimens under optical microscopy (OM). The measured porosities were displayed on Figure 4 with different abscissas. Generally, as the energy density E increases, the porosity decreases to a minimum value in Group 10 and then rebounds slightly to Group 7. As shown in Figure 3, the metallurgical defects are remarkably diverse, and their shapes become more and more irregular with increasing porosity. In comparison with Figures 2a and 4b, the tensile quantities of σ_y, σ_u, and ε_t basically have an opposite trend to the porosity with varying E values. At last, Figure 4c enumerates the detail L-PBF parameters of Groups 1~10 for AMed Ti-6Al-4V.

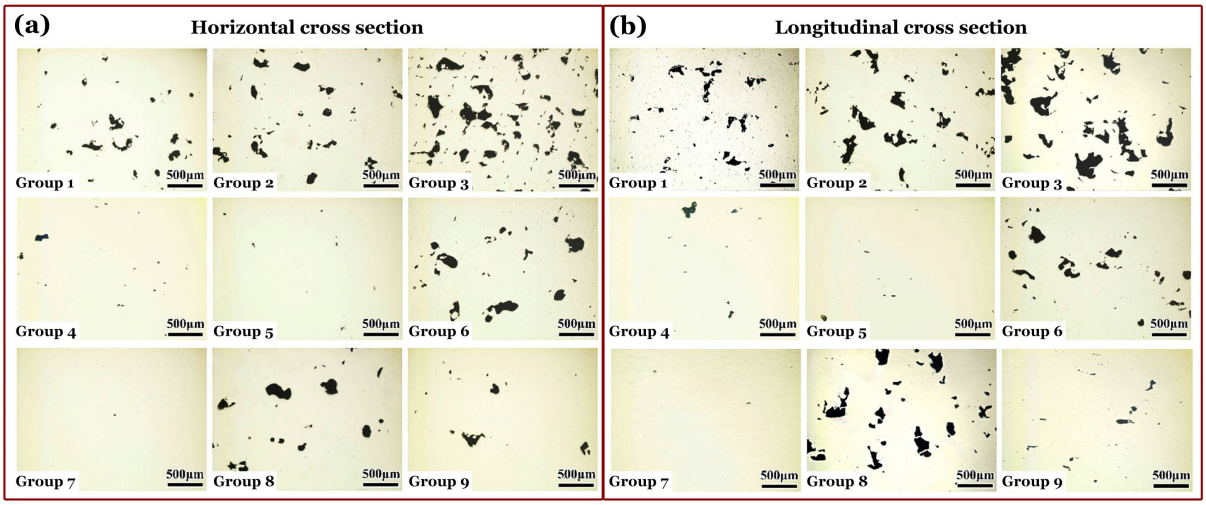

Figure 3. Selected optical micrographs [23] showing metallurgical defect distributions on horizontal (**a**) and longitudinal (**b**) cross sections of specimens from Groups 1~9.

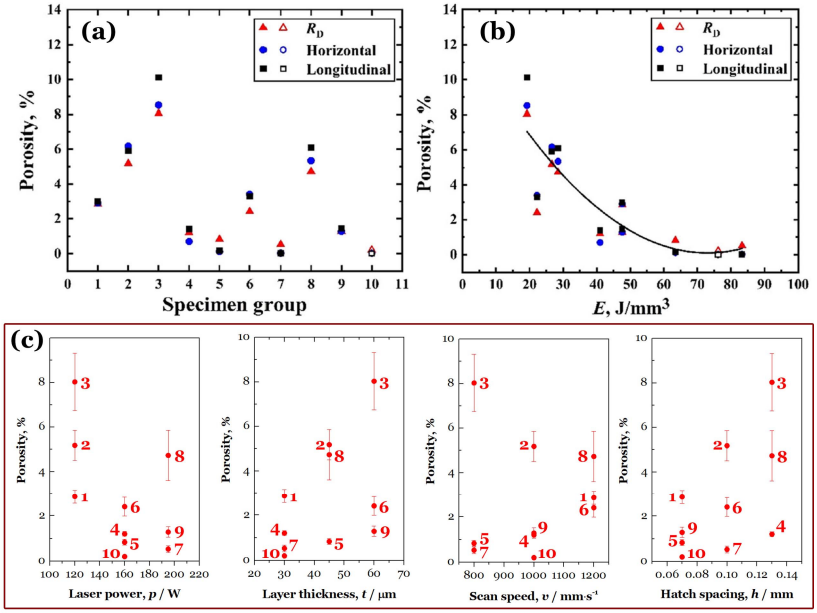

Figure 4. (**a**) Porosity versus specimen group. (**b**) Porosity versus volumetric energy density E. (**c**) Porosity versus laser power p, layer thickness t, scan speed v, and hatch spacing h; red numbers denote Groups 1~10 [23].

3.2. Basic Features of 3D Printed Microstructures

Figure 5 presents the typical OM microstructure of AMed titanium alloys via L-PBF [16,51]. Figure 5a has an almost equiaxed microstructure (EM) of prior β grains on the cross section perpendicular to the building direction, and Figure 5b has almost columnar prior β grains on the cross section parallel to the building direction. Within the grain boundary, depicted with dashes in Figure 5, the prior β phase has transformed to the lamellae of α and β, which constitutes lamellar microstructure (LM). The neighboring lamellae with a similar crystallographic orientation have stacked one by one to form an LM colony. Along the building direction, many LM colonies have piled up to a columnar grain of the prior β phase.

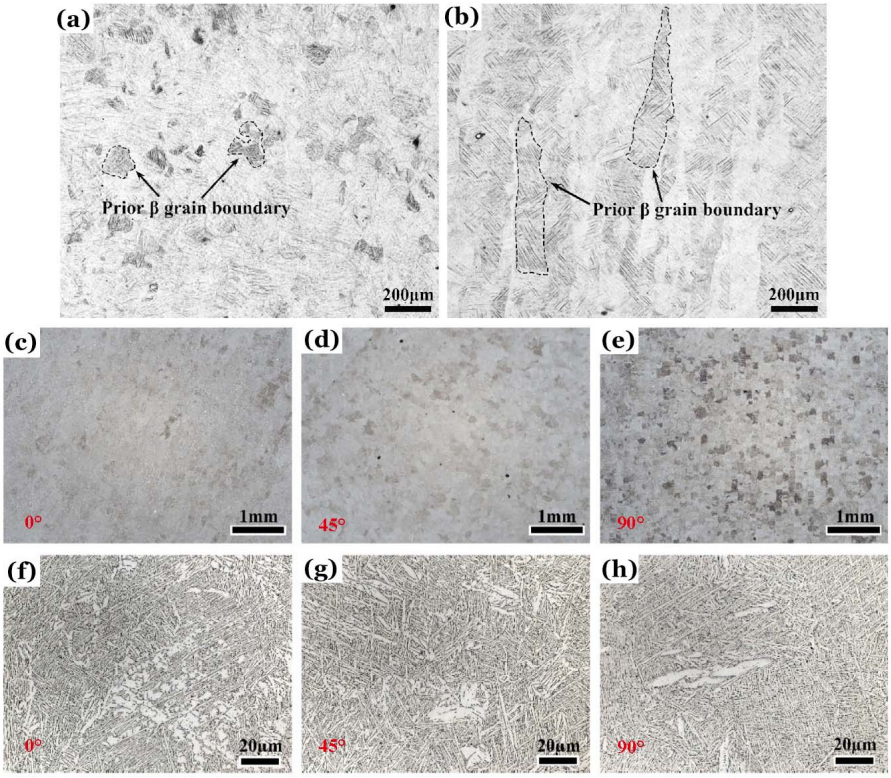

Figure 5. Optical metallographic images [51] on horizontal (**a**) and longitudinal (**b**) cross sections of specimens from Group 10. Optical metallographic images [16] on cross sections perpendicular to the specimen axes for another additively manufactured Ti-6Al-4V with different orientations of 0°, 45° and 90° at low magnification (**a**–**e**) and at high magnification (**f**–**h**).

Figure 5c–h is for an AMed Ti-6Al-4V with different orientations of 0°, 45°, and 90° [16] by using another combination of PBF parameters and after heat treatment of an annealing, named Group 11. Their OM images show the microstructures on the cross sections perpendicular to the oriented specimen axes at low and high magnification. As the angle of orientation increases from 0° to 90°, a global EM morphology gradually emerges on the cross sections from Figure 5c with blurred domains to Figure 5e with clear grains of prior β. For the enlarged OM images of Figure 5f–h, within the LM domains, there do not appear to be any significant differences in the cross sections for the oriented specimens, except for the presence of coarsened lamellar grains.

According to the traditional classification [1,2] of microstructural morphologies for the α + β typed titanium alloys, there are four basic microstructures: (1) EM of equiaxed α grains and transformed β domains [52], (2) LM of lamellar α and β grains [53], (3) bimodal microstructure (BM) of equiaxed α grains and LM domains [54], (4) basket weave (BW) microstructure of lamellar α and β grains with irregular orientations. Figure 5f–h shows

an example of OM images for the BW microstructure. These four microstructures can be obtained by many specific thermal–mechanical processing procedures.

3.3. Thermal–Mechanical Evolution of Defect and Microstructure

One of the major advantages of AM is the ease with which printed specimens with complex configurations can be manufactured, but that also limits the possibility of further mechanical processing. For example, the complex shapes cannot be rolled, forged, stamped and so forth [55]. This leaves hot isostatic pressing (HIP) as the most popular method of thermal–mechanical processing for the AMed specimens.

In the HIP process, the specimens are simultaneously subjected to both high temperatures and high isostatic pressures using a gaseous transfer medium. The main factor that distinguishes HIP from other processing techniques is the use of gas as a pressure transfer medium to induce equivalent changes in three dimensions in the material it surrounds. For a successful HIP, three variables must be properly controlled: temperature, pressure, and time [56].

Figures 6 and 7 give an example to describe the effect of HIP on the AMed microstructure and metallurgical defects of the specimen. Chi et al. [57,58] vertically printed two batches of specimens for an AMed Ti-6Al-4V via L-PBF, which were subsequently heat-treated for 2 h at 710 °C in a vacuum and then cooled in an argon atmosphere. This parameter combination of the PBF processing and the annealing was named as Group 12, in which one batch was selected to further post-treat with a HIP at 920 °C and 1000 bar for 2 h in argon atmosphere. As a control group, the other batch of specimens has no post processing. Figure 6 shows a characterization of electron backscatter diffraction (EBSD) for a very local region around an AM defect on a cross section cut from these specimens of Group 12 without HIP. No difference was observed in the local microstructure of the defect edges from that of the LM or BW matrix. Figure 7 gives a visual comparison of the EBSD morphologies for the AMed matrix after the heat treatment (Group 12) and then with (Figure 7a,b) or without (Figure 7c,d) this HIP treat.

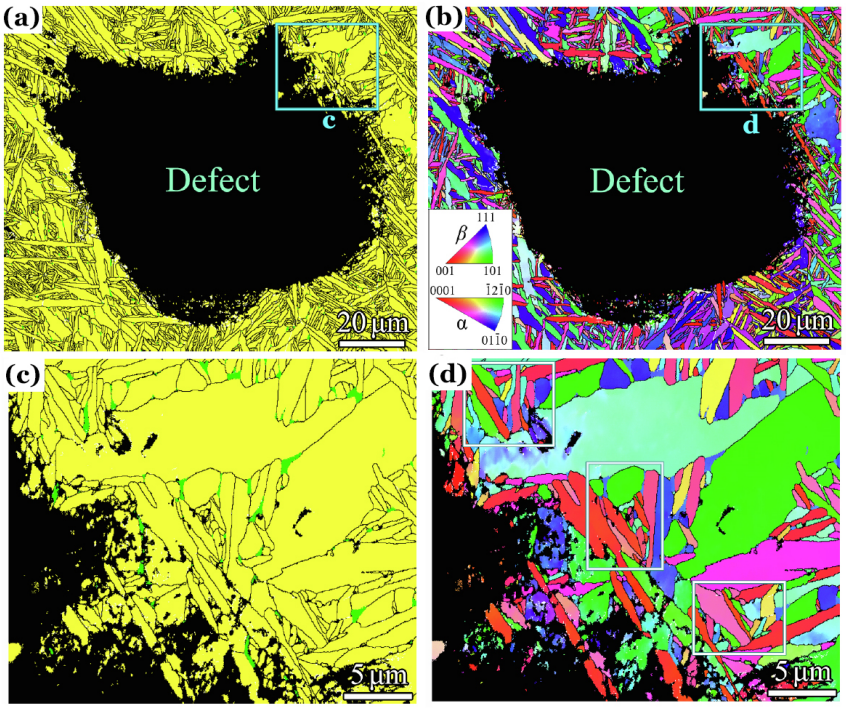

Figure 6. Electron backscatter diffraction (EBSD) for an additively manufactured titanium alloy with Group 12 of processing parameters via laser powder bed fusion and experienced through annealing [57]: (**a**) Phase map, yellow for α and cyan for β; (**b**) Inverse pole figure (IPF) showing crystallographic orientations of α and β grains. (**c**,**d**) enlarging boxes c and d in (**a**,**b**).

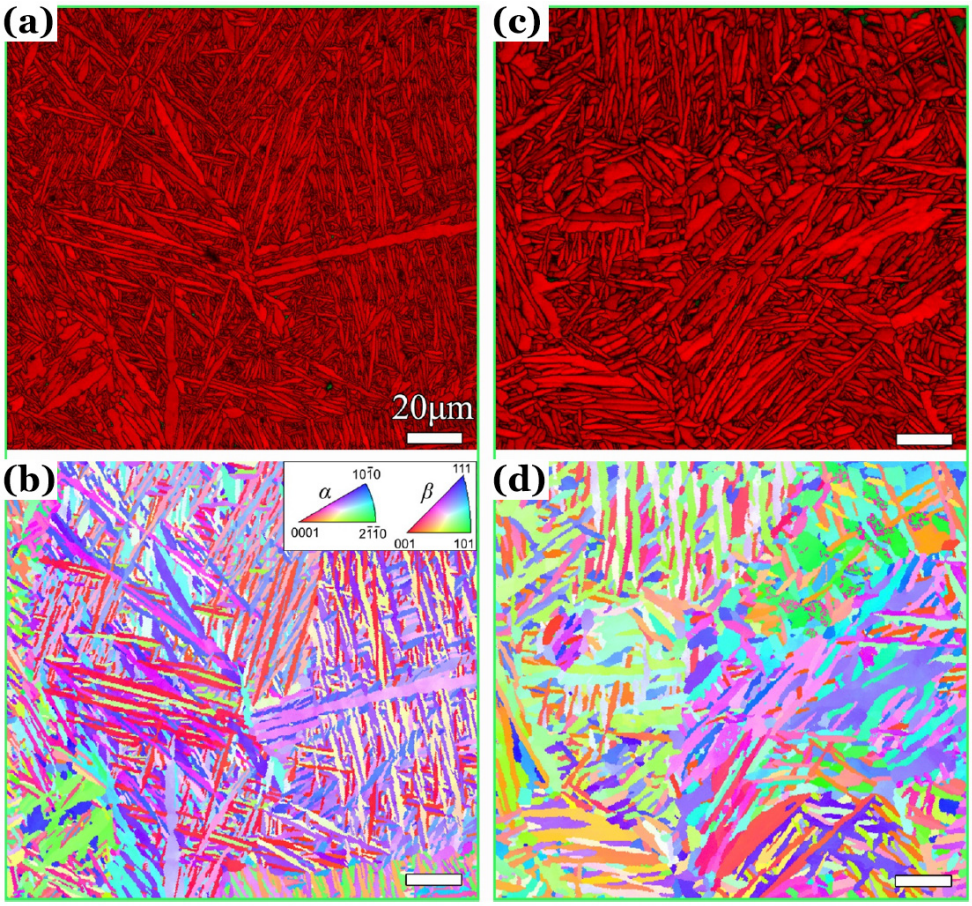

Figure 7. Electron backscatter diffraction (EBSD) for specimens from Group 12 without (**a**,**b**) and with (**c**,**d**) a treatment of hot isostatic pressing (HIP) [58]: (**a**,**c**) Phase maps, red for α and green for β; (**b**,**d**) inverse pole figures (IPFs). The white scale bars all represent 20 μm.

In general, the main purpose of HIP is focused on the effectiveness in eliminating the void-types of metallurgical defects, and the side effect is equivalent to performing additional heat treatment, which will coarsen the AMed microstructure. For Group 12, along the building direction, the tensile properties of the specimens without HIP [57] are σ_y = 951 MPa and σ_u = 1007 MPa, and the elongation is about 14% at fracture. Comparatively, the specimens with HIP [58] are σ_y = 849 MPa, σ_u = 946 MPa, and a longer elongation. This is attributed to the additional annealing of the HIP, i.e., at 920 °C for 2 h.

4. Fatigue Behaviors in High-Cycle and Very-High-Cycle Regimes

4.1. S-N Data and Curves

Figure 8 shows S-N data and curves for AMed Ti-6Al-4V alloys via L-PBF with different combinations of processing parameters, heat treatments, surface states, and building orientations. The abscissa is the failure cycle N_f, and the ordinate is the applied stress amplitude σ_a. All fatigue tests were conducted at room temperature and in ambient air by axial cycling at an ultrasonic frequency of 20 k ± 500 Hz.

Figure 8a is for the combinations of Groups 1~10 under stress ratios $R = -1$ [23]. The fatigue specimens of Groups 1~10 were vertically printed to hourglass shapes; after heat treatment, the specimens were ground and polished to the final dimensions [23,51]. Figure 8b is for vertically printed specimens with a combination Group 13 of L-PBF parameters of p = 325 W, t = 0.03 mm, v = 1300 mm/s, h = 0.12 mm, and E = 69.44 J/mm^3 [59], then stress relieved by heating at 600 °C for 2 h. Along the building direction, the Vickers hardness is 367 HV, and σ_y = 1068 MPa, σ_u = 1202 MPa. The fatigue specimens were divided into two batches: one retained the directly printed rough surface, called As-built, and

the other had a polished surface, called Polished. Figure 8c is for Group 11 [16]. The fatigue specimens were printed with orientations of 0°, 45°, and 90°, and the tensile properties along these orientations were not reported in Ref. [16].

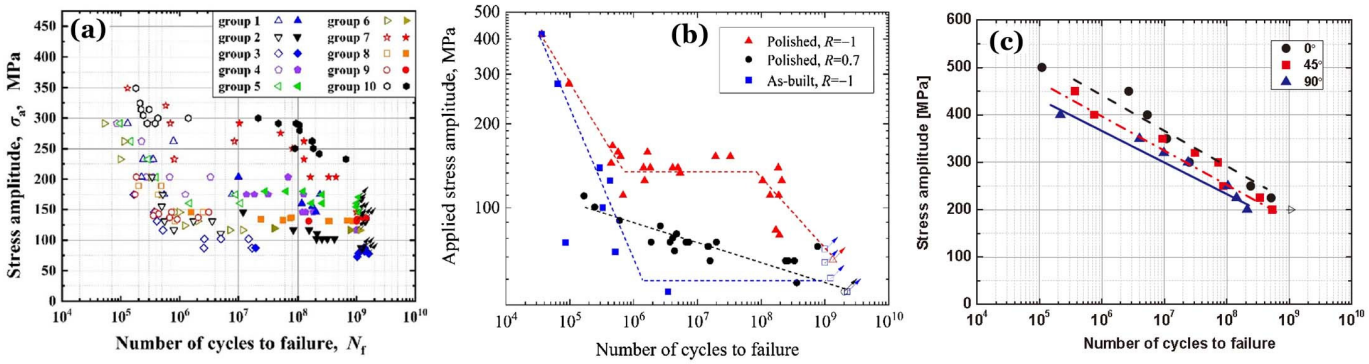

Figure 8. S-N data and curves in terms of stress amplitude: (**a**) Groups 1~10 at stress ratio $R = -1$ [23], hollow and solid symbols denoting surface and internal crack initiation, respectively; (**b**) Group 13 with different surface states at $R = -1$ and 0.7 [59]; (**c**) Group 11 with building orientations of 0°, 45°, and 90° [16]. Symbols with arrows represent runout specimens, solid or dashed lines correspond to the approximate fits for data points of the same colors.

4.2. Specimens with Different Surface States

The S-N curve of As-built specimens for Group 13 has a slope in a high-cycle regime ($N < 10^7$ cycles) and a horizontal asymptote at a negative stress ratio of $R = -1$. All specimens failed by high-cycle fatigue (HCF, $N_f < 10^7$ cycles) while $\sigma_a > 80$ MPa and either failed in the HCF stage or survived beyond 10^9 cycles while $\sigma_a < 80$ MPa. No VHCF occurs.

The S-N curve of Polished specimens for Group 13 has two slopes in high-cycle and very-high-cycle regimes, respectively, at $R = -1$, and changes to a single slope from HCF to VHCF at $R = 0.7$. The fatigue strengths at 10^7 cycles are $\sigma_{a7} = 130$ MPa at $R = -1$ and $\sigma_{a7} = 80$ MPa at $R = 0.7$. VHCF can occur at both stress ratios of $R = -1$ and 0.7.

For Group 13, Figure 9a,b of OM images presents the AM defect distributions on the horizontal cross sections of As-built and Polished specimens with metallographic etching. There is a defect-enriched layer with an offset distance T inward from the surface for both As-built and Polished specimens due to different AM strategies for surface and inner filling, as shown in Figure 1a. Figure 9c–f shows the representative morphologies of fatigue fracture surfaces imaged by scanning electron microscopy (SEM). Figure 9c,d is for HCF of As-built specimens, in which fatigue failure was induced by cooperative interactions of directly printed rough surface and subsurface-enriched defects. Figure 9e,f gives an example of VHCF for Polished specimens; the enriched subsurface defects still appeared on the fracture surface, as shown in Figure 9e, and the final failure originated from a subsurface defect, as shown in Figure 9f.

It should be noted that although the fatigue cracks lead to the final failure initiated from the edge of the subsurface defect, this does not indicate that the failure type of the AMed specimens can be classified as a surface one. In fact, the classification of failure types should be based on the overall macroscopic fractography rather than on some local fracture characteristics [60].

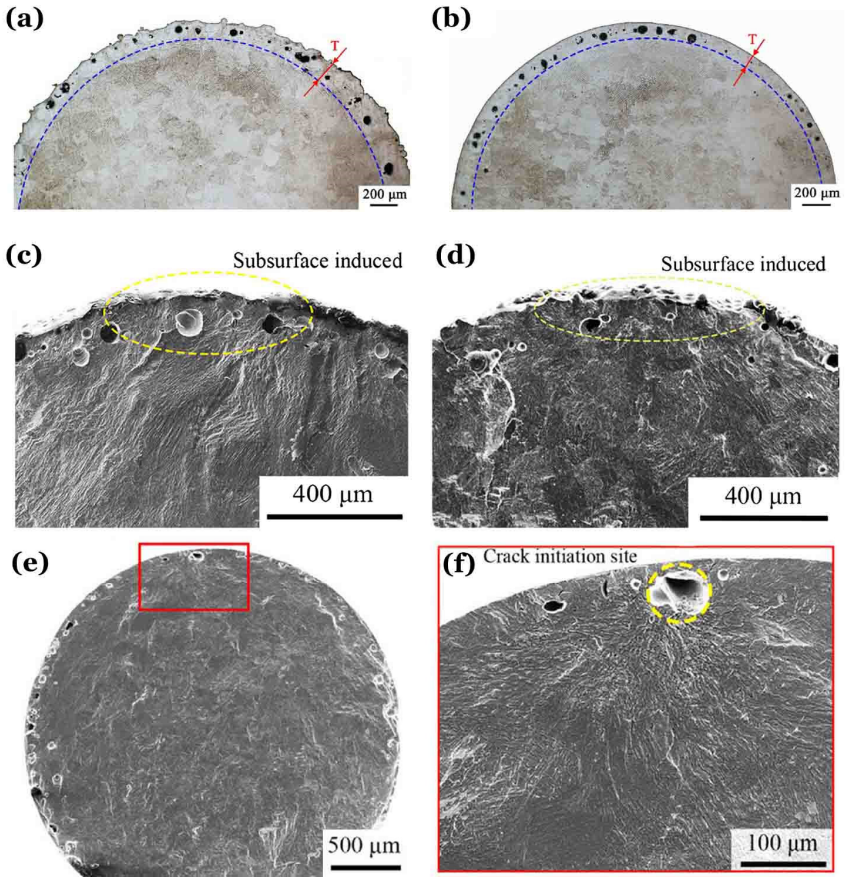

Figure 9. Optical metallographic images on horizontal cross section of As-built (**a**) and Polished (**b**) specimens. Scanning electron micrographs for fatigue fracture surfaces of As-built (**c**,**d**) and Polished (**e**,**f**) specimens, (**f**) enlarging box in (**e**). (**a**) $R = -1$, $\sigma_a = 139.1$ MPa, $N_f = 2.9 \times 10^5$ cycles; (**b**) $R = -1$, $\sigma_a = 125.2$ MPa, $N_f = 4.3 \times 10^5$ cycles; (**c**) $R = -1$, $\sigma_a = 153$ MPa, $N_f = 3.3 \times 10^7$ cycles [59].

4.3. Specimens with Different Processing Parameters

For Groups 1~10 of different L-PBF parameters, in Figure 8a, the hollow and solid symbols represent fatigue failure induced by surface and internal crack initiation. Fatigue performances are optimized with decreasing porosity of Groups 1~10, and single S-N characteristics become duplex or stepwise at a negative stress ratio of $R = -1$. The fatigue strength at 10^7 cycles from $\sigma_{a7} = 75$ MPa is enhanced to 300 MPa. Figure 10 demonstrates typical morphologies of fatigue crack initiation for different failure types. Figure 10a,b depict SEM images for HCF induced by specimen surface and a surface defect, respectively. Figure 10c depicts an SEM image for VHCF induced by an irregular void-typed defect at the specimen subsurface caused by the AM process. Figure 10d schematically draws the possible formation process of this AM defect. Figure 10e,f of SEM images is for VHCF induced by subsurface AM defects with different shapes or types.

Figure 9a,b also presents an EM of prior β grains distributed on the cross sections perpendicular to the building direction. Their equivalent diameters are in the same order of magnitude as the transverse dimensions of columnar grains as dashed in Figure 5a,b. Consequently, the yield strength and UTS of As-built and Polished specimens for Group 13 are close to those for Group 10. However, their fatigue performance varies greatly in both HCF and VHCF regimes. The fatigue strength of As-built specimens is only comparable to that of specimens for Group 3 with the highest porosity in HCF and VHCF regimes. The HCF strength of Polished specimens is between those of specimens with the second and third highest porosity for Groups 2 and 8, and the VHCF strength is even lower than the latter two. This indicates that the weakening of fatigue strength, especially in the VHCF

regime, is attributed, firstly, to the directly printed rough surface and, secondly, to the subsurface-enriched defects in the AMed specimens of titanium alloys.

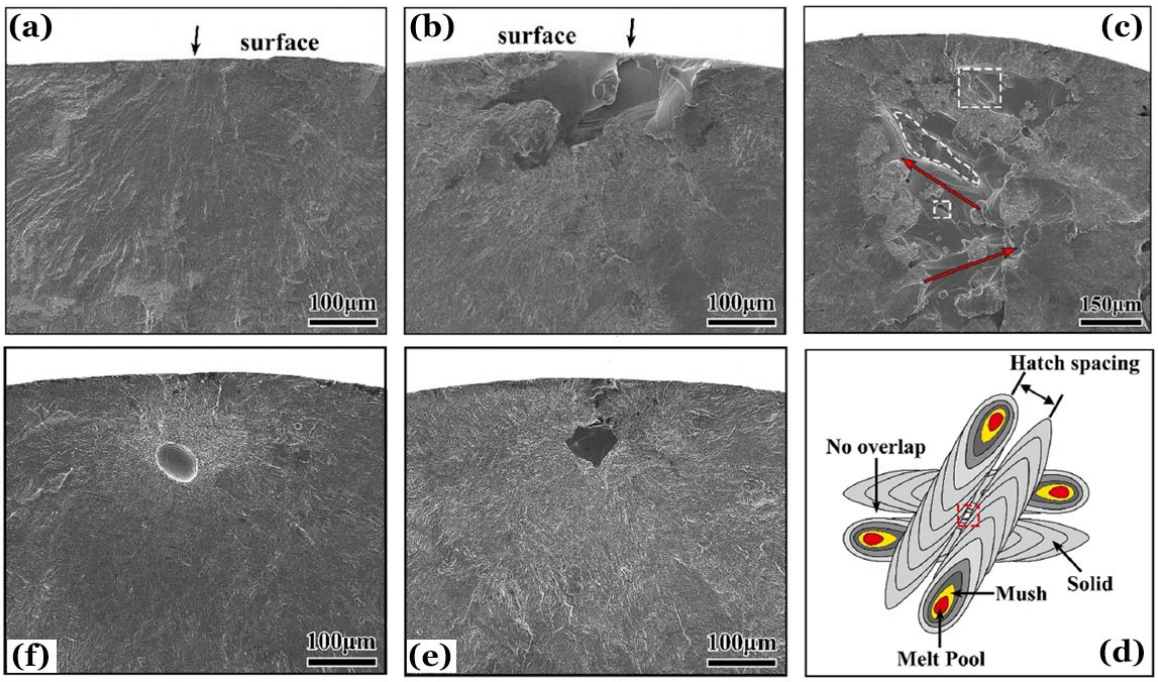

Figure 10. Typical morphologies for fatigue crack initiation at stress ratio $R = -1$: (**a**) Group 7, σ_a = 291 MPa, $N_f = 6.95 \times 10^5$ cycles; (**b**) Group 5, σ_a = 175 MPa, $N_f = 8.93 \times 10^6$ cycles; (**c**) Group 2, σ_a = 116 MPa, $N_f = 1.56 \times 10^8$ cycles; (**d**) schematic of melting pools without overlap; (**e**) Group 1, σ_a = 174 MPa, $N_f = 2.38 \times 10^8$ cycles; (**f**) Group 7, σ_a = 262 MPa, $N_f = 1.28 \times 10^8$ cycles [23].

4.4. Internal Crack Initiation with Different Building Orientations

For Group 11 with orientations 0°, 45°, and 90°, the fatigue specimens were coaxially machined from the heat-treated round bars of AMed Ti-6Al-4V and then ground to the final hourglass shapes. In the range of 200 MPa $\leq \sigma_a \leq$ 500 MPa, all specimens failed by internal crack initiation in HCF and VHCF regimes regardless of failure cycles. The S-N curves show continuously decreasing slopes with low data scatter. Basically, the specimens with 0° orientation had the best fatigue resistance, followed by 45° and 90°, although the differences in their values are inconsiderable.

Figure 11 provides the representative SEM morphologies of crack initiation for these specimens, in which the main cracks originated from the AM defects at the specimen interior. There appears to be a certain orientation relationship between these critical AM defects that lead to the ultimate fatigue fracture. The AM defect in Figure 11a can be tilted 45° to obtain the defect in Figure 11b and then tilted a further 45° to obtain the defect in Figure 11c. They also seem to be interpreted by Figure 10d. Figure 11d–f give alternative situations for other metallurgical defects with different shapes or AM types.

The AM defects in Group 11 have projected areas on the fracture surfaces of about the same order of magnitude as those in Group 1, as shown in Figure 10e. In comparison to the crack initiation behaviors mentioned above, the location of fatigue origin tends to be the specimen interior (Group 11) rather than on the directly printed rough surface, polished surface, subsurface-enriched defects (As-built and Polished specimens of Group 13), or other subsurface defects (Group 1~10) as the depth of the layer removed from the specimen surface increases. As a result, the fatigue resistance of Group 11 is much better than that of Groups 1~10 and 13. Even for Group 10, which has the lowest porosity, its HCF resistance is significantly lower than that of Group 11.

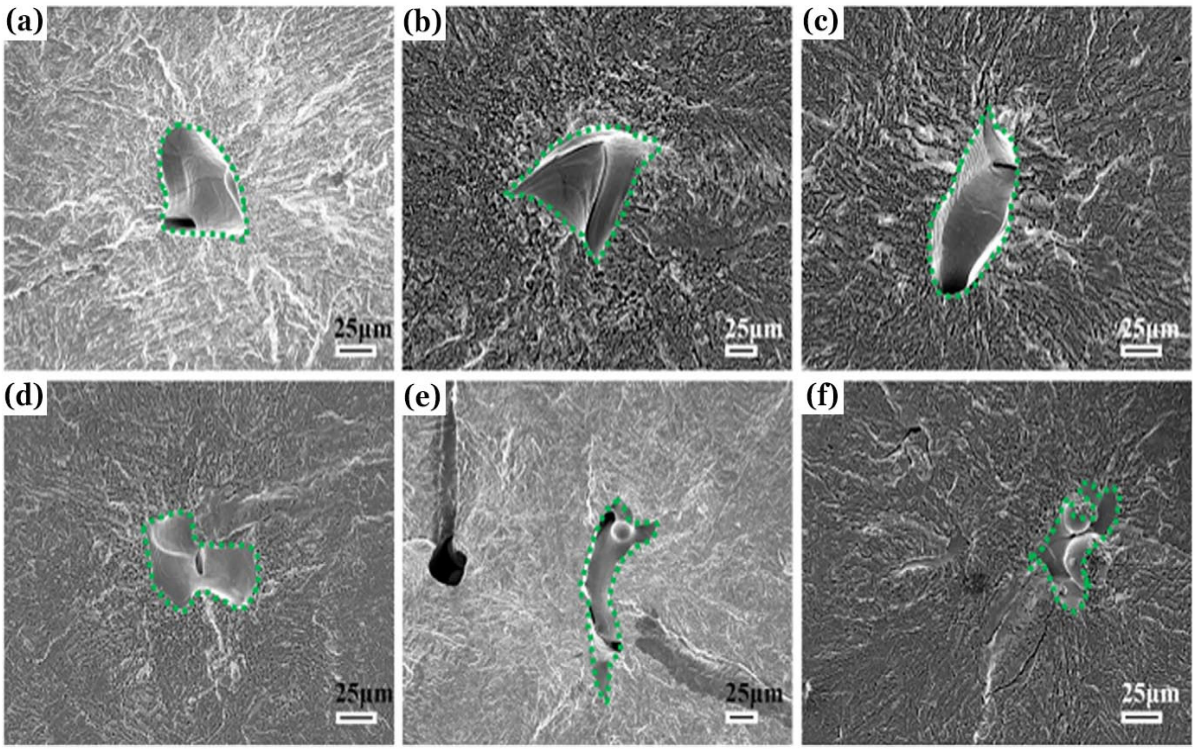

Figure 11. Internal origins of fatigue crack initiation for specimens of Group 11 with orientations 0°, 45° and 90° at stress ratio $R = -1$: (**a**) 0°, σ_a = 400 MPa, $N_f = 5.35 \times 10^6$ cycles; (**b**) 45°, σ_a = 225 MPa, $N_f = 3.39 \times 10^8$ cycles; (**c**) 90°, σ_a = 350 MPa, $N_f = 3.99 \times 10^6$ cycles; (**d**) 0°, σ_a = 300 MPa, $N_f = 2.51 \times 10^7$ cycles; (**e**) 45°, σ_a = 400 MPa, $N_f = 7.55 \times 10^5$ cycles; (**f**) 90°, σ_a = 320 MPa, $N_f = 9.81 \times 10^6$ cycles [16].

5. Effect of Stress Ratio on Fatigue Strength and Fractography

5.1. S-N Data with Various Stress Ratios

Fu et al. [61] vertically printed a batch of round bars for an AMed Ti-6Al-4V by using L-PBF with the same parameters of processing and heat treatment as Group 13. The porosity is 2.93%, and the tensile properties are σ_y = 1191 MPa, 1246 MPa, and ε_t = 5.6% along the building direction. The fatigue specimens were coaxially machined from the round bars, then ground and polished to hourglass shapes for ultrasonic push–pull and pull–pull cycling at a loading frequency of 20 k ± 500 Hz in ambient air and at room temperature. These specimens were named as Group 14.

Figure 12 shows the S-N data in terms of the applied maximum stress σ_{max} for the AMed Ti-6Al-4V alloys with different L-PBF processing and heat treatments of Groups 10 (Figure 12a), 14 (Figure 12b) and 12 (Figure 12c) under various stress ratios of $R = -1$, −0.5, 0.1, 0.2 and 0.5.

For Group 10 of Figure 12a, in the range of 300 MPa $\leq \sigma_{max} \leq$ 800 MPa, the S-N data exhibit a continuous decreasing shape for the failure life from 10^5 to 10^9 cycles. While σ_{max} > 500 MPa, two specimens were tested and failed by surface crack initiation-induced HCF; while σ_{max} < 500 MPa, six specimens were tested; one ran out, and others failed by internal crack initiation-induced VHCF. At σ_{max} = 500 MPa, two specimens were tested, one failed by surface crack-induced HCF and the other by internal crack-induced VHCF.

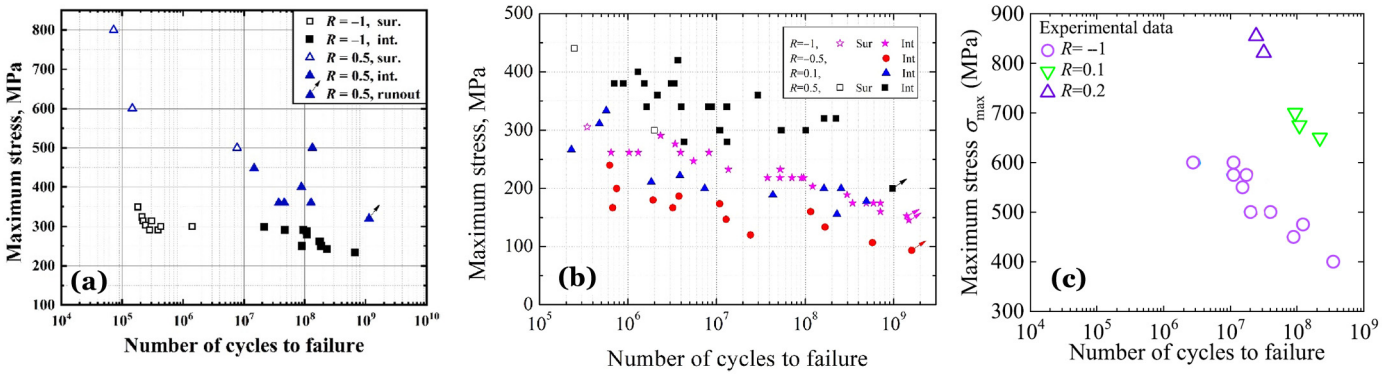

Figure 12. S-N data in terms of maximum stress for additively manufactured Ti-6Al-4V alloys under negative and positive stress ratio *R*: (**a**) Group 10 at $R = -1$ and 0.5 [51]; (**b**) Group 14 at $R = -1$, -0.5, 0.1 and 0.5 [61]; (**c**) Group 12 at $R = -1$, 0.1 and 0.2 [57]. Sur: surface crack initiation-induced final fatigue failure; Int: internal crack initiation-induced final fatigue failure. Symbols with arrows representing runout specimens.

5.2. Crack Initiation Morphologies for Case-I

For Group 14 of Figure 12b, the fatigue resistance in terms of maximum stress first decreases and then increases as the stress ratio of the *R* value increases. For $R = -1$, -0.5, 0.1, and 0.5, the specimens under $R = 0.5$ have the highest σ_{max}, $R = -1$ the second, $R = 0.1$ the third, and $R = -0.5$ the lowest. All fatigue specimens that failed in the VHCF regime were classified as internal crack initiation.

While $R = -1$, 25 specimens were tested, two ran out of 10^9 cycles, 21 failed by internal crack initiation-induced VHCF or HCF, and only one failed by surface crack initiation-induced fatigue failure at $N_f = 3 \times 10^5$ cycles under $\sigma_{max} > 300$ MPa, which has the shortest N_f and the highest σ_{max}. While $R = -0.5$, thirteen specimens were tested, one ran out of 10^9 cycles at $\sigma_{max} < 100$ MPa, and the other twelve failed in HCF or VHCF regime caused by internal crack initiation in the range of 100 MPa $< \sigma_{max} <$ 250 MPa. While $R = 0.1$, 11 specimens were tested, and all fatigue failed by internal crack initiation in HCF and VHCF from 2×10^5 to 5×10^8 cycles, regardless of failure life. While $R = 0.5$, twenty-four specimens were tested, one ran out of 10^9 cycles at $\sigma_{max} = 200$ MPa, and the others preferred (18/19) internal crack initiation in the range of 300 MPa $< \sigma_{max} <$ 400 MPa.

Figure 13a–l offers representative SEM images of crack initiation and growth morphologies on the fracture surface for selected specimens that failed in different fatigue regimes and stress ratios. In these subfigures, the crack that leads to the final fatigue failure was originated from an AM defect, which was yellow dashed and marked as LOF. To be exact, the defect is not LoF but a type of AM pore that Fu et al. [61] had mislabeled.

For the negative stress ratios of $R = -1$ and -0.5, a crack initiation region of rough area (RA) incubates, nucleates, and matures at $N_f > 10^8$ cycles as the fatigue life grows around the AM defect. The RA regions are circular or elliptical in shape and tangent to the specimen surfaces, as shown in Figure 13c,f. As the stress ratio increases to $R = 0.1$, a large RA region can be formed at 10^7 cycles $< N_f < 10^8$ cycles, as shown in Figure 13h, the boundary of which is not tangent to the specimen surface and the projected area of which is even larger than the RA at $N_f > 10^8$ cycles as shown in Figure 13i. While the stress ratio further increases to $R = 0.5$, around the dominating AM defect, which causes the final failure, no identifiable RA region was observed on the fracture surface even at $N_f > 10^8$ cycles, as shown in Figure 13j–l. This crack initiation behavior with the RA region is quite similar to that with the fine granular area (FGA, [62]) in high-strength steels under negative and positive *R* values [63].

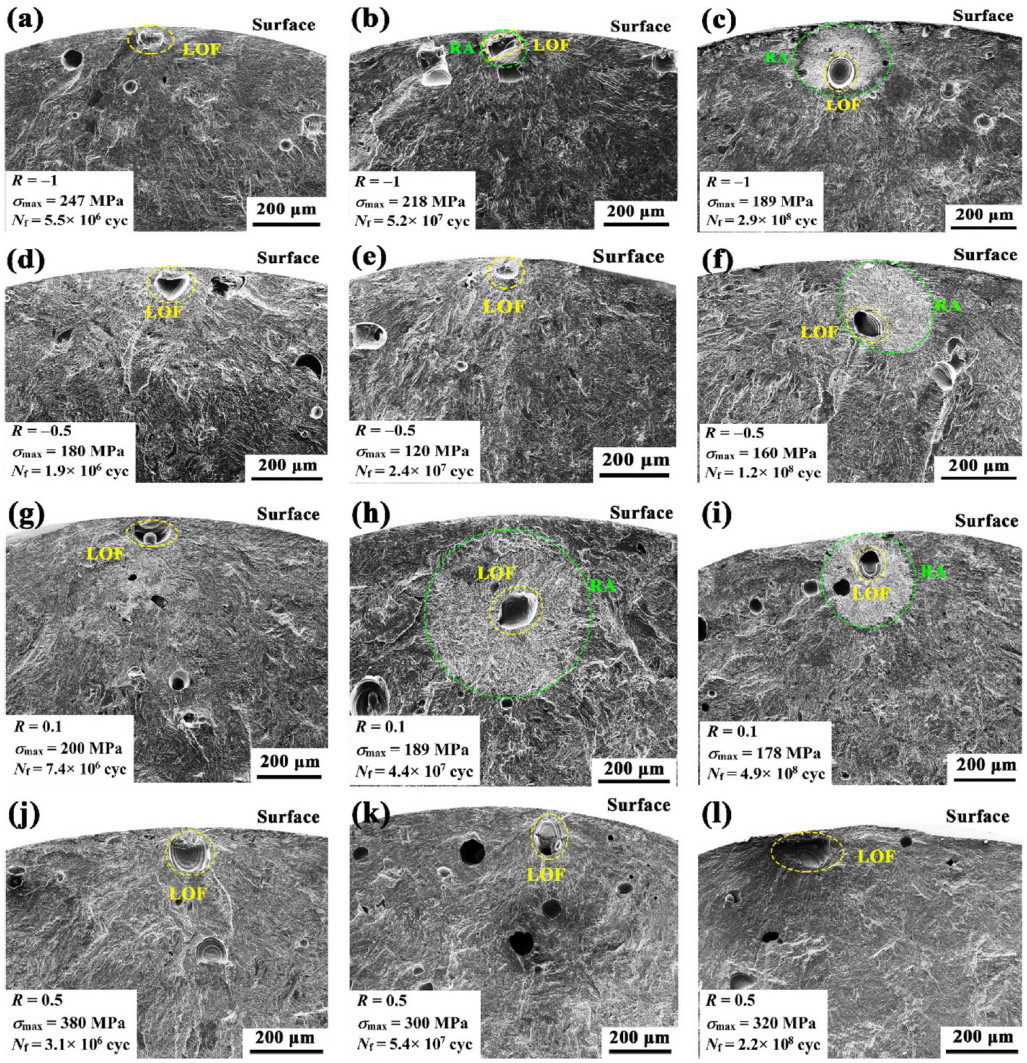

Figure 13. Scanning electron micrographs showing crack initiation and growth regions of selected fatigue specimens (**a**–**l**) for Group 14 under different stress ratios and loading cycles. LOF: lack-of-fusion typed defect, RA: rough area of crack initiation region [61].

5.3. Crack Initiation Morphologies for Case-II

For Group 10 of the AMed Ti-6Al-4V, Figure 14 displays the typical SEM images for crack initiation in HCF and VHCF under negative and positive stress ratios of $R = -1$ and 0.5. Figure 14a is for surface crack initiation-induced HCF, which originated from a surface AM defect. Figure 14b,c is for internal crack initiation-induced VHCF at $R = -1$, which originated from a subsurface AM defect and encircled by an RA region with granular morphology. Figure 14d–i gives two examples showing the whole fracture surface (Figure 14d,g) and the detailed region of fatigue crack initiation and early propagation, which originated from an internal AM defect and cracking of a leaf-like facet (Figure 14e,f,h,i) for failure lives of 10^7 and 10^8 cycles at $R = 0.5$. Obviously, for a positive stress ratio of $R = 0.5$, the crack initiation morphologies of Group 10, as shown in Figure 14d–i, are very different from those of Group 14, as shown in Figure 13k,l, which is defined as Case-I. In contrast, the former case of fatigue crack initiation for Group 10 is defined as Case-II.

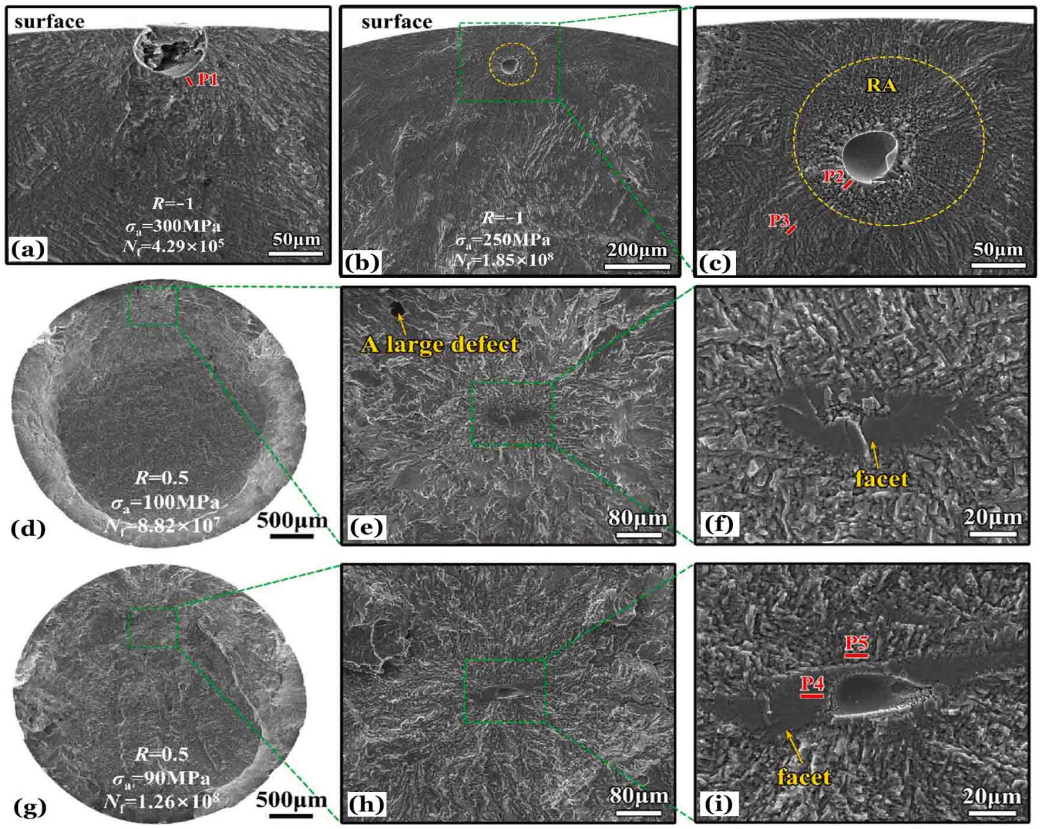

Figure 14. Typical morphologies of scanning electron microscopy for fatigue crack initiation and growth on fracture surfaces in high-cycle and very-high-cycle regimes under negative (**a**–**c**) and positive (**d**–**i**) stress ratios. Red bars P1, P2, P3, P4, and P5 are locations of TEM (transmission electron microscopy) samples cut by FIB (focused ion beam) milling [51].

In Figure 14, the red bars of P1, P2, P3, P4, and P5 locate the lamellae for further characterization of the profile microstructure underneath the fracture surface by using transmission electron microscopy (TEM). The lamellae were cut from the representative locations on the fracture surfaces with the milling of a focused ion beam (FIB). P1 is for a core region around a surface AM defect of crack initiation experienced HCF at $R = -1$; P2 and P3 are for locations near and away from the crack initiation site of a subsurface AM defect experienced VHCF at $R = -1$; P2 is within the RA region and P3 outs; P4 and P5 are for locations near the internal AM defect of crack initiation experienced VHCF at $R = 0.5$; P4 is within the facet; and P5 is outs but adjacent. The microstructures on TEM lamellae of P1, P3, P4, and P5 almost keep the original AMed LM or BW with coarse grains of α and β phases. On top of the TEM lamella of P2, there is a nanograin layer [51] with a heterogeneous refined microstructure [64] of twisted lamellar α/β grains and equiaxed grains, which may be produced by recrystallization.

Similar phenomena of nanograin formation and microstructure refinement can also occur in other metallic materials, whether conventional manufacturing [63,65–68] or AM [15,61,69]. Hong et al. [63] proposed a model of numerous cyclic pressing (NCP) to explain these phenomena, in which fracture surface nanocrystallization occurs and is associated with VHCF initiation under negative stress ratios due to a very long process ($N > 10^7$ cycles) of repeated crack opening and closing. This process can assume and store a massive amount of cyclic strain energy, which is introduced by the applied stress amplitude, thus allowing the material to have a relatively high σ_a value. The key to the NCP model is a sufficient number of load cycles and a sufficiently high value of the compressive stress component.

5.4. Fatigue Strength Estimation under Tensile Mean Stress

Figure 15 of Haigh diagrams [70] quantitatively delineates the effect of tensile mean stress or stress ratio on the fatigue resistance of an AMed Ti-6Al-4V alloy in comparison of high-strength steels and titanium alloys with several microstructures based on the relations of Goodman [71], Gerber [72] and Pan et al. [65]. Figure 15a,b is for the AMed titanium alloy of Group 14 [61] in the HCF and VHCF regime, respectively. Figure 15c is for the VHCF limit of high-strength steel [73]. Figure 15d,e is for a Ti-6Al-4V alloy with EM [74] in HCF and VHCF regimes, respectively. Figure 15f is for the VHCF limit of titanium alloys with LM, BM, or EM.

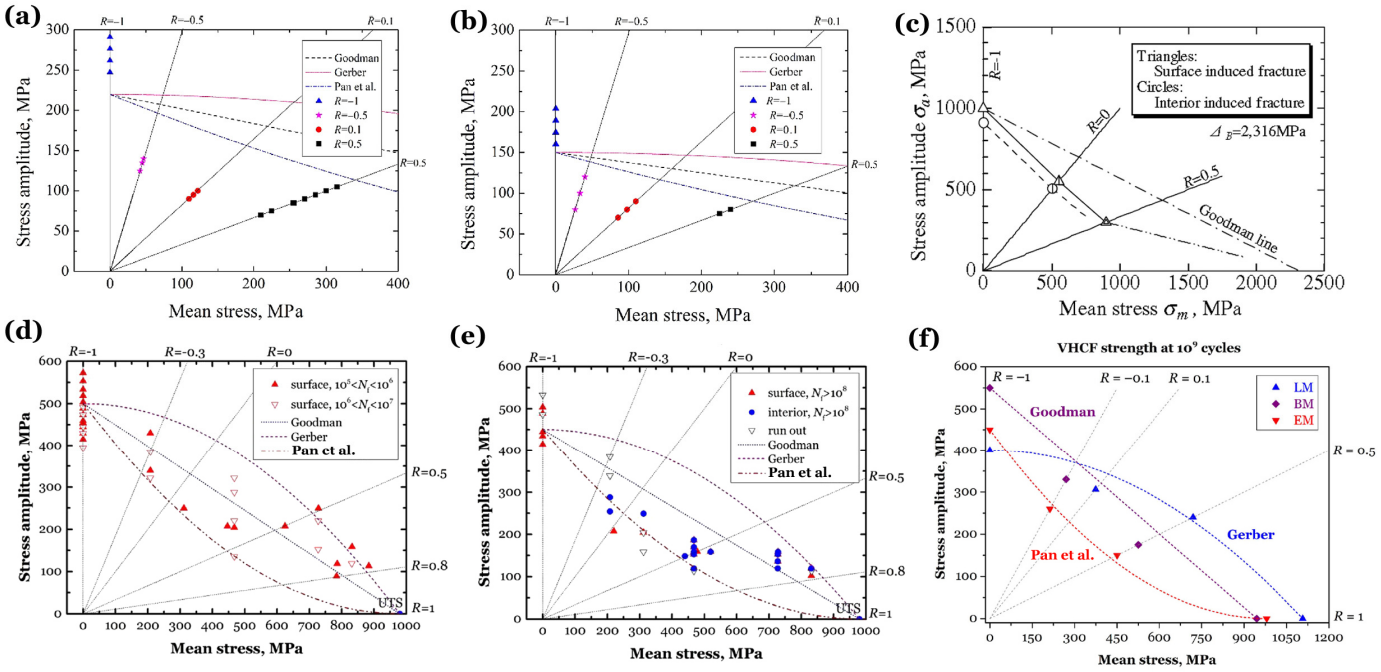

Figure 15. Haigh diagrams for an additively manufactured Ti-6Al-4V of Group 14 [61] for the following: (**a**) 1×10^6 cycles $< N_f < 8 \times 10^6$ cycles; (**b**) 1×10^8 cycles $< N_f < 7 \times 10^8$ cycles. (**c**) Haigh diagram for very-high-cycle fatigue limit of a high-strength steel [73]. Haigh diagrams for a titanium alloy [74] with equiaxed microstructure (EM) at (**d**) 10^7 cycles and (**e**) 10^9 cycles. (**f**) Haigh diagram for titanium alloys [54] with lamellar microstructure (LM), bimodal microstructure (BM), or EM.

For both HCF and VHCF regimes, the fatigue strength of the AMed titanium alloy degrades sharply from the stress ratio of $R = -1$ to 0.5, worse than that of a mill-annealed titanium alloy with EM [74]. We noticed that the AMed alloys and high-strength steels have many similarities [75], e.g., the nonmetallic inclusions [76,77] in high-strength steels play a similar role in inducing fatigue crack initiation and early growth, as do the AM defects in AMed alloys. Sakai et al. [73] proposed a bilinear model to describe the stress ratio effect on the VHCF limit of σ_a with varying mean stress σ_m in high-strength steel. Following the analogy of inclusions and AM defects, this model can be transferred to AMed alloys from high-strength steel.

The AMed titanium alloy is often with a microstructure of LM or BW. For the conventionally manufactured titanium alloys, Figure 15d–f depicts how microstructure affects the effect of tensile mean stress σ_m and stress ratio R on fatigue strength. For the EM, HCF and VHCF strengths deteriorate with increasing σ_m in accordance with a Goodman line and Pan et al. [65,74]'s under-convex curve, respectively. On the "true" fatigue limit [30,31] beyond 10^9 cycles, crack initiation in an LM domain [53] abides by a Gerber up-convex curve, and the BM [54] follows a Goodman line, which can be regarded as a mixed microstructure of LM and EM.

6. Discussion of Promising Methods to Improve Fatigue Property

6.1. Influences of Heat Treatment and Hot Isostatic Pressing

Figure 16a presents S-N data and curves for Ti-6Al-4V alloys with a BM [78] and several AMed microstructures [79] subjected to HCF and VHCF with axial cycling at an ultrasonic frequency of 20 [78] and 19 kHz [79] under $R = -1$ at room temperature and in ambient air. The BM has tensile properties of σ_y = 920 MPa, σ_u = 1010 MPa, and ε_t = 17.5%, named Heinz [78]. An AMed Ti-6Al-4V was produced via L-PBF with processing parameters of p = 175 W, t = 0.03 mm, v = 710 mm/s, h = 0.12 mm, and E = 68.47 J/mm^3 by using a SLM (selective laser melting) 250^{HL} system to obtain a batch of raw cylinders. Then, the cylinders were divided into two groups: one named SLM-1b, which was heat treated at 800 °C for 2 h in argon atmosphere, and the other named SLM-2, which was HIP treated at 920 °C for 2 h at 1000 bar in an argon atmosphere. The other AMed Ti-6Al-4V was produced via an electron beam PBF (EB-PBF)—also called an electron beam melting (EBM) [80]—with processing parameters of acceleration voltage 60 kV, maximum current 21 mA, t = 0.05 mm, v = 4530 mm/s, h = 0.1 mm. An Arcam A2X system is used to obtain a batch of raw cylinders without any post-treatment. This batch was designated EBM. All specimens of the AMed Ti-6Al-4V alloys were machined from the raw cylinders by turning along the building direction.

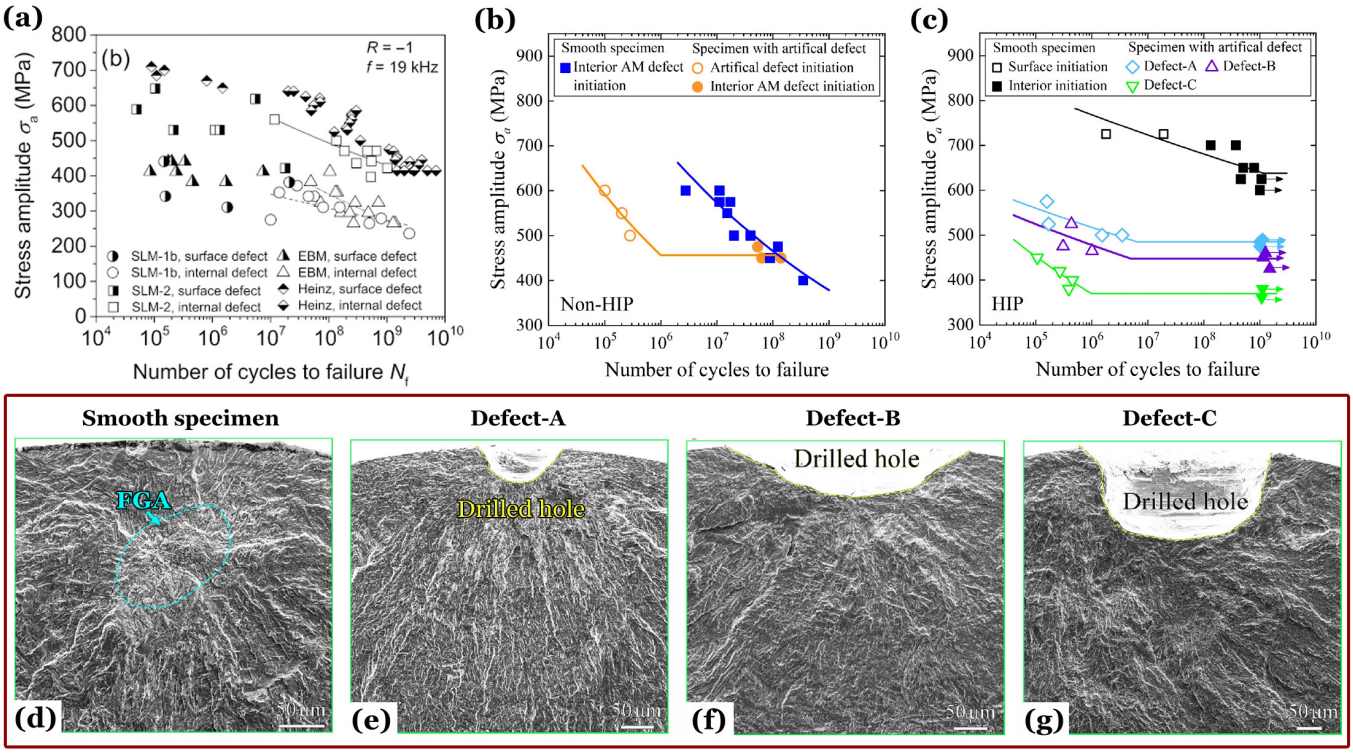

Figure 16. (**a**) S-N data and curves for titanium alloys produced by methods of additive and conventional manufacturing [78,79]. S-N curves at $R = -1$ for an additively manufactured Ti-6Al-4V of Group 12 [58] without (**b**) and with (**c**) a treatment of hot isostatic pressing (HIP). Symbols with arrows representing runout specimens. Fatigue fracture surfaces of HIP specimens failed at the following: (**d**) σ_a = 700 MPa, $N_f = 1.32 \times 10^8$ cycles; (**e**) σ_a = 525 MPa, $N_f = 1.69 \times 10^5$ cycles; (**f**) σ_a = 525 MPa, $N_f = 4.34 \times 10^5$ cycles; (**g**) σ_a = 420 MPa, $N_f = 2.69 \times 10^5$ cycles [58].

In the range of 400 MPa < σ_a < 700 MPa, the conventionally manufactured Ti-6Al-4V with BM of Heinz [78] maintains the maximum HCF and VHCF strengths than SLM-2, EBM, and SLM-1b; The HCF and VHCF strengths for HIP specimens of SLM-2 are the second for the corresponding range of 400 MPa < σ_a < 600 MPa; EBM and SLM-1b are the third and the minimum in the range of 250 MPa < σ_a < 450 MPa. In the VHCF regime,

fatigue damage preferentially initiates from internal defect, and S-N data and curves can be easily categorized into two groups, from high to low-stress amplitude of σ_a and from long to short fatigue life of N_f. The VHCF resistance of SLM-2 is slightly less than that of the BM; they both greatly exceed that of EBM and SLM-1b, and the resistance of SLM-1b is also slightly less than that of EBM. In the HCF regime, fatigue damage preferentially initiates from surface defect, and S-N data can be categorized into four groups: the BM, SLM-2, EBM, and SLM-1b from high to low-stress amplitude of σ_a, and from long to short fatigue life of N_f.

It is easy to see that HIP significantly improves the fatigue properties of AMed titanium alloys, especially in VHCF. This improvement can be attributed to two factors: the coarsening of AMed microstructure and the elimination of void-typed defects.

For AMed Ti-6Al-4V, annealing can also produce a coarsened LM or BW microstructure, which enhances the ductility by reducing the tensile strength. Groups 10, 12, and 14 give examples. Group 14 has the optimum fatigue performance and the best tensile plasticity. In fact, due to the presence of void-typed AM defects, the fatigue strength is strongly dependent on some quantities of fatigue short or long crack growth [81,82], similar to fracture toughness, which is more appropriately related to local plasticity [83] and can be directly assessed by tensile strength and ductility.

6.2. Competitions among Metallurgical and Artificial Defects

Chi et al. [58] investigated the HCF and VHCF behaviors of smooth specimens and the specimens with artificial defects for an AMed Ti-6Al-4V of Group 12 without and with a HIP treatment, as shown in Figure 16b,c. All fatigue specimens were tested, at room temperature and in air, by ultrasonic axial cycling at a loading frequency of 20 k $\pm$ 500 Hz with a stress ratio of $R = -1$.

For specimens without HIP, in the range of 500 MPa $\leq \sigma_a \leq$ 600 MPa, fatigue cracks tend to nucleate from the edges of the artificial surface defects for 1×10^5 cycles $\leq N_f \leq 3 \times 10^5$ cycles, and from the AM defects at specimen interior for 3×10^6 cycles $\leq N_f \leq 5 \times 10^7$ cycles. While $\sigma_a <$ 500 MPa, all failed specimens were internally cracked by interior AM defects inducing VHCF, despite specimens with or without artificial defects.

For specimens with HIP, the smooth specimens perform very well in both HCF and VHCF regimes. While $\sigma_a >$ 700 MPa, two specimens were tested, and all failed by surface crack initiation; one failed at about $N_f = 2 \times 10^6$ cycles, and the other failed at about $N_f = 2 \times 10^7$ cycles. In the range of 600 MPa $< \sigma_a <$ 700 MPa, seven specimens were tested; two ran out of 10^9 cycles, the other five failed by internal crack initiation inducing VHCF, and Figure 16d gives an SEM example for the fracture surface. Simultaneously, all specimens with artificial defects failed in the HCF regime, no VHCF occurred, and the fatigue cracks all originated from the drilled holes on specimen surfaces, as shown in Figure 16e–g, which were named Defect-A, Defect-B, and Defect-C.

In Figure 16d, a crack initiation area with a rough fracture surface was identified as a dashed ellipse, which had been mislabeled FGA by Chi et al. [58], and the correct name should be RA. Within the RA region, no AM defect of the void types can be determined on the fracture surface. In Figure 16e–g, around the artificial defects, there is no discernible region of crack initiation and early growth.

Attributed to the presence of artificial defects, the fatigue strength of the drilled specimens is significantly lower than that of the smooth specimens and continues to decrease as the defect size increases. The VHCF limit at 10^9 cycles was measured as σ_a = 625 MPa for the smooth specimens, σ_a = 490 MPa for specimens with Defect-A, σ_a = 460 MPa for Defect-B, and σ_a = 380 MPa for Defect-C. For the smooth specimens of Group 12 with HIP, the fatigue performance is even better than the BM without any AM defects which is produced by conventional manufacturing.

6.3. Roles of Microstructure, Local Plastiticity, Tensile Strength and Ductility

It is very reasonable that the fatigue behavior of AMed materials can be modulated by adjusting the defect size [84,85]. This is exactly the same as for high-strength steels, except that the AM defects [15,18] were replaced by the nonmetallic inclusions [28] or other inhomogeneities [86–88] and can be easily described by Kitagawa-Takahashi diagrams [89].

For the AMed microstructure of Group 12 with HIP treatment, fatigue crack initiation occurs from the matrix and sustains a VHCF limit of σ_a = 625 MPa in the absence of void-typed AM defects and other artificial defects. Even if an AM defect with an equivalent size of Defect-C exists in the specimen interior, the AMed matrix with HIP still can endure a VHCF limit of σ_a = 380 MPa, which is greater than that of the AMed Ti-6Al-4V of Groups 1~11, 13 and 14 without HIP treatment. This is because the additional annealing introduced by HIP actually coarsens the AMed microstructure.

As mentioned in Section 6.1, the coarsening of AMed microstructure also plays a key role in fatigue performance, especially in very-high-cycle regimes. It is noted that, for materials with void-typed defects, coarsening of the microstructure is not required, and simply increasing the local plasticity of the defect edges can make a substantial improvement in fatigue properties.

For titanium alloys, the local plasticity depends on the local microstructure and can be enhanced by methods of microstructural design [52,54,90–95], e.g., tension [52], torsion [92] and compression with or without recrystallization annealing. This method is not only applicable to the symmetrically cyclic tension and compression ($R = -1$) but may also be applied to a wider range of working conditions. Specifically, the VHCF crack initiation in the LM domain [53] with increasing tensile mean stress approximately obeys a Gerber relation for $-1 < R \leq 0.5$ [54], which is consistent with the case in AMed aluminum alloys [96,97]. In the result of Du et al. [51], the AM defect causes the surrounding LM domain cleavage to form a lamellar facet as the VHCF origin and leads to the final fatigue fracture at $R = 0.5$. Therefore, we can shield the AM defect itself by regulating the microstructure around the AM defect to optimally dominate the VHCF behavior of the AMed materials at $R > -1$.

We can utilize the micro and/or nano tests, such as microhardness and nanoindentation [98–100], to provide a better assessment of the local microstructure and plasticity. However, it is always difficult to acquire detailed information on local microstructure and plasticity around the AM defects, so we also often use global quantities to estimate the potential fatigue resistance of AMed Titanium alloys. Tensile strength and ductility are the most popularly used global quantities for structural materials.

Figure 17 displays the several tensile curves of engineering stress versus engineering strain under quasi-static monotonic loading of titanium alloys produced by methods of AM and conventional manufacturing. The tensile properties rely mainly on the global microstructure rather than the distribution of metallurgical defects when the porosity is not very large. As shown in Figure 17a, in comparison with a titanium alloy with EM of equiaxed ($\alpha + \beta$), the microstructure of acicular α' martensite makes a higher strength and a lower plasticity. After an annealing, the martensite will transform to a microstructure of coarse lamellar ($\alpha + \beta$) with a downgraded strength and upgraded ductility. Xu et al. [101] tailored the microstructure of ultrafine lamellar ($\alpha + \beta$) to simultaneously achieve superior tensile properties of AMed Ti-6Al-4V than the conventional one. Chong et al. [102] developed a technique of rapid heat treatment that can globally enhance the tensile strength and ductility of a Ti-6Al-4V with fully martensitic microstructures, as shown in Figure 17b. More recently, Qu et al. [103] used HIP treatment to remove void-typed defects, followed by heat treatment to modulate the microstructure, and claim to have achieved the highest HCF strength to date. This is an example of the potential viability of this approach.

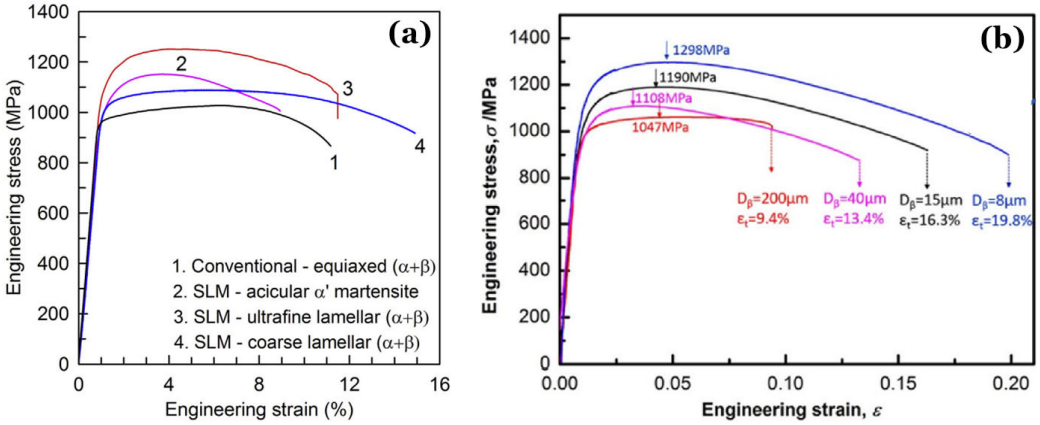

Figure 17. Simultaneous enhancement of tensile strength and ductility for Ti-6Al-4V produced by methods of additive [101] (**a**) and conventional [102] (**b**) manufacturing.

7. Summary and Perspectives

In this paper, based on our previous works, we have reviewed the characteristics of additively manufactured (AMed) Ti-6Al-4V alloys and the current status of fatigue research in the high-cycle and very-high-cycle regimes, as shown in Table 1, to summarize and rank the main factors affecting fatigue properties and discuss the effect of stress ratio on fatigue strength and fractography.

Table 1. Ranking of main factors dominating very-high-cycle fatigue and the possible solutions.

Rank	Dominating Factor	Possible Solution
1	Large porosity	Optimization of AM parameters
2	As-built roughed specimen surface	Machining and/or polishing
3	Big void-typed defects	Hot isostatic pressing
4	Trade-off between strength and plasticity	Microstructure design

By using AM, AMed titanium alloys can easily achieve high-strengths, even for the commercially used Ti-6Al-4V, an α + β type, whereas metastable β types are required by conventional methods. For optimized AM parameters, the directly printed state has the highest strength and not optimal plasticity. In very-high-cycle regimes, fatigue strength is related to both tensile strength and ductility. If the AM parameters are not optimized, the primary factor influencing fatigue performance is porosity, which tends to be a high value. When the porosity is relatively low, surface roughness, e.g., the as-built specimen surface, becomes an important influence, followed by the maximum size of metallurgical defects on the projection plane perpendicular to the loading direction. These factors are also dependent on plasticity, and their influence decreases as ductility increases. As a result, the AMed titanium alloys often exhibit higher values of very-high-cycle fatigue strength after an equivalent annealing of thermal–mechanical treatments than the directly printed state. However, annealing will inevitably reduce the strength of the AMed material, which in turn will reduce its fatigue strength. In this way, the trade-off relationship between strength and plasticity can be reproduced to very-high-cycle fatigue. Therefore, those methods that can simultaneously improve the strength and plasticity of titanium alloys also hold promise for improving very-high-cycle fatigue strength.

Author Contributions: Conceptualization, X.P.; Data curation, R.F., L.D. and X.P; Investigation, C.G., Y.Z., J.J. and X.P.; Methodology, X.P.; Project administration, C.G. and X.P.; Resources, R.F., L.D. and X.P.; Supervision, C.G., Y.Z., J.J. and X.P.; Visualization, X.P.; Writing—original draft, C.G., Y.Z. and X.P.; Writing—review and editing, X.P. All authors have read and agreed to the published version of the manuscript.

Funding: This research was funded by Youth Doctoral Fundation Project of Harbin University, grant number HUDF2021106.

Acknowledgments: C.G. is very grateful to Harbin University for the financial support.

Conflicts of Interest: Author Yang Zhang was employed by the company China Construction Sixth Engineering Division Co., Ltd. The remaining authors declare that the research was conducted in the absence of any commercial or financial relationships that could be construed as a potential conflict of interest.

References

1. Lütjering, G.; Williams, J. *Titanium*, 2nd ed.; Springer: Berlin, Germany, 2003.
2. Leyens, C.; Peters, M. *Titanium and Titanium Alloys*; Wiley-VCH Verlag: Weinheim, Germany, 2003.
3. Gibson, I.; Rosen, D.; Stucker, B.; Khorasani, M. *Additive Manufacturing Technologies*, 3rd ed.; Springer: Cham, Switzerland, 2021.
4. DebRoy, T.; Wei, H.L.; Zuback, J.S.; Mukherjee, T.; Elmer, J.W.; Milewski, J.O.; Beese, A.M.; Wilson-Heid, A.; De, A.; Zhang, W. Additive manufacturing of metallic components—Process, structure and properties. *Prog. Mater. Sci.* **2018**, *92*, 112–224. [CrossRef]
5. Liu, Z.Z.; Zhou, Q.H.; Liang, X.K.; Wang, X.B.; Li, G.C.; Vanmeensel, K.; Xie, J.X. Alloy design for laser powder bed fusion additive manufacturing: A critical review. *Int. J. Extreme Manuf.* **2024**, *6*, 022002. [CrossRef]
6. Su, J.L.; Jiang, F.L.; Teng, J.; Chen, L.Q.; Yan, M.; Requena, G.; Zhang, L.C.; Wang, Y.M.; Okulov, I.; Zhu, H.M.; et al. Recent innovations in laser additive manufacturing of titanium alloys. *Int. J. Extrem. Manuf.* **2024**, *6*, 032001. [CrossRef]
7. Javidrad, H.; Koc, B.; Bayraktar, H.; Simsek, U.; Gunaydin, K. Fatigue performance of metal additive manufacturing: A comprehensive overview. *Virtual Phys. Prototy.* **2024**, *19*, e2302556. [CrossRef]
8. Badoniya, P.; Srivastava, M.; Jain, P.K.; Rathee, S. A state-of-the-art review on metal additive manufacturing: Milestones, trends, challenges and perspectives. *J. Braz. Soc. Mech. Sci.* **2024**, *46*, 339. [CrossRef]
9. Luo, X.; Yang, C.; Li, D.D.; Zhang, L.C. Laser powder bed fusion of beta-type titanium alloys for biomedical application: A review. *Acta Metall. Sin. Engl.* **2024**, *37*, 17–28. [CrossRef]
10. Leary, M. *Design for Additive Manufacturing*; Elsevier: Amsterdam, The Netherlands, 2020.
11. Guo, N.; Leu, M.C. Additive manufacturing: Technology, applications and research needs. *Front. Mech. Eng.* **2013**, *8*, 215–243. [CrossRef]
12. Yap, C.Y.; Chua, C.K.; Dong, Z.L.; Liu, Z.H.; Zhang, D.Q.; Loh, L.E.; Sing, S.L. Review of selective laser melting: Materials and applications. *Appl. Phys. Rev.* **2015**, *2*, 041101. [CrossRef]
13. Behvar, A.; Haghshenas, M.; Djukic, M.B. Hydrogen embrittlement and hydrogen-induced crack initiation in additively manufactured metals: A critical review on mechanical and cyclic loading. *Int. J. Hydrogen Energy* **2024**, *58*, 1214–1239. [CrossRef]
14. Chua, C.; Liu, Y.T.; Williams, R.J.; Chua, C.K.; Sing, S.L. In-process and post-process strategies for part quality assessment in metal powder bed fusion: A review. *J. Manuf. Syst.* **2024**, *73*, 75–105. [CrossRef]
15. Pan, X.; Du, L.; Qian, G.; Hong, Y. Microstructure features induced by fatigue crack initiation up to very-high-cycle regime for an additively manufactured aluminium alloy. *J. Mater. Sci. Technol.* **2024**, *173*, 247–260. [CrossRef]
16. Qian, G.; Li, Y.; Paolino, D.S.; Tridello, A.; Berto, F.; Hong, Y. Very-high-cycle fatigue behavior of Ti-6Al-4V manufactured by selective laser melting: Effect of build orientation. *Int. J. Fatigue* **2020**, *136*, 105628. [CrossRef]
17. Zhao, Q.; Sun, Q.; Xin, S.; Chen, Y.; Wu, C.; Wang, H.; Xu, J.; Wan, M.; Zeng, W.; Zhao, Y. High-strength titanium alloys for aerospace engineering applications: A review on melting-forging process. *Mater. Sci. Eng. A* **2022**, *845*, 143260. [CrossRef]
18. Sanaei, N.; Fatemi, A. Defects in additive manufactured metals and their effect on fatigue performance: A state-of-the-art review. *Prog. Mater. Sci.* **2021**, *117*, 100724. [CrossRef]
19. Dowling, N.E. *Mechanical Behavior of Materials: Engineering Methods for Deformation, Fracture, and Fatigue*, 4th ed.; Pearson: Boston, MA, USA, 2013.
20. Ashby, M.F. *Materials Selection in Mechanical Design*, 5th ed.; Butterworth-Heinemann: Oxford, UK, 2016.
21. Hertzberg, R.W.; Vinci, R.P.; Hertzberg, J.L. *Deformation and Fracture Mechanics of Engineering Materials*, 6th ed.; Wiley: Oxford, UK, 2020.
22. Reed, R.; Smith, J.; Christ, B. *The Economic Effects of Fracture in the United States*; National Institute of Standards and Technology: Gaithersburg, MD, USA, 1983.
23. Du, L.; Qian, G.; Zheng, L.; Hong, Y. Influence of processing parameters of selective laser melting on high-cycle and very-high-cycle fatigue behaviour of Ti-6Al-4V. *Fatigue Fract. Eng. Mater. Struct.* **2021**, *44*, 240–256. [CrossRef]
24. Schijve, J. *Fatigue of Structures and Materials*, 2nd ed.; Springer: Dordrecht, Germany, 2009.
25. Bathias, C.; Paris, P. *Gigacycle Fatigue in Mechanical Practice*; Marcel Dekker: New York, NY, USA, 2005.
26. Thijs, L.; Verhaeghe, F.; Craeghs, T.; Humbeeck, J.; Kruth, J. A study of the microstructural evolution during selective laser melting of Ti-6Al-4V. *Acta Mater.* **2010**, *58*, 3303–3312. [CrossRef]
27. Suresh, S. *Fatigue of Materials*, 2nd ed.; Cambridge University Press: Cambridge, UK, 1998.
28. Murakami, Y. *Metal Fatigue: Effect of Small Defects and Nonmetallic Inclusions*; Elsevier: Oxford, UK, 2002.
29. Wöhler, A. Wöhler's experiments on the strength of metals. *Engineering* **1867**, *4*, 160–161.
30. Furuya, Y. 10^{11} gigacycle fatigue properties of high-strength steel. *ISIJ Int.* **2021**, *61*, 396–400. [CrossRef]

31. Furuya, Y.; Shimamura, Y.; Takanashi, M.; Ogawa, T. Standardization of an ultrasonic fatigue testing method in Japan. *Fatigue Fract. Eng. Mater. Struct.* **2022**, *45*, 2415–2420. [CrossRef]
32. *ASTM E468-90*; Standard Practice for Presentation of Constant Amplitude Fatigue Test Results for Metallic Materials. ASTM Int.: Conshohocken, PA, USA, 2004.
33. Atrens, A.; Hoffelner, W.; Duerig, T.W.; Allison, J.E. Subsurface crack initiation in high cycle fatigue in Ti6Al4V and in a typical martensitic stainless steel. *Scr. Metall.* **1983**, *17*, 601–606. [CrossRef]
34. Murakami, Y.; Nomoto, T.; Ueda, T.; Murakami, Y. On the mechanism of fatigue failure in the superlong life regime ($N > 10^7$ cycles), Part I: Influence of hydrogen trapped by inclusions. *Fatigue Fract. Eng. Mater. Struct.* **2000**, *23*, 893–902. [CrossRef]
35. Murakami, Y.; Nomoto, T.; Ueda, T.; Murakami, Y. On the mechanism of fatigue failure in the superlong life regime ($N > 10^7$ cycles), Part II: A fractographic investigation. *Fatigue Fract. Eng. Mater. Struct.* **2000**, *23*, 903–910. [CrossRef]
36. Bathias, C. There is no infinite fatigue life in metallic materials. *Fatigue Fract. Eng. Mater. Struct.* **1999**, *22*, 559–565. [CrossRef]
37. Lukáš, P.; Kunz, L. Specific features of high-cycle and ultra-high-cycle fatigue. *Fatigue Fract. Eng. Mater. Struct.* **2002**, *25*, 747–753. [CrossRef]
38. Sakai, T. Review and prospects for current studies on very high cycle fatigue of metallic materials for machine structural use. *J. Solid Mech. Mater. Eng.* **2009**, *3*, 425–439. [CrossRef]
39. Hong, Y.; Sun, C. The nature and the mechanism of crack initiation and early growth for very-high-cycle fatigue of metallic materials—An overview. *Theor. Appl. Fract. Mech.* **2017**, *92*, 331–350. [CrossRef]
40. Hong, Y.; Hu, Y.; Zhao, A. Effects of loading frequency on fatigue behavior of metallic materials—A literature review. *Fatigue Fract. Eng. Mater. Struct.* **2023**, *46*, 3077–3098. [CrossRef]
41. Zerbst, U.; Beretta, S.; Köhler, G.; Lawton, A.; Vormwald, M.; Beier, H.T.; Klinger, C.; Černý, I.; Rudlin, J.; Heckel, T.; et al. Safe life and damage tolerance aspects of railway axles—A review. *Eng. Fract. Mech.* **2013**, *98*, 214–271. [CrossRef]
42. Zhao, J.C.; Wan, J.; Zhang, S.Z.; Yan, C.L.; Zhao, H.W. Application of ultrasonic fatigue technology in very-high-cycle fatigue testing of aviation gas turbine engine blade materials: A review. *Sci. China Technol. Sci.* **2024**, *67*, 1317–1363. [CrossRef]
43. Celli, D.A.; Scott-Emuakpor, O.; Warner, J.; George, T. Investigation of self-heating during ultrasonic fatigue testing and effect on very high cycle fatigue behavior of titanium 6Al-4V. *J. Eng. Gas Turb. Power—ASME* **2023**, *145*, 031016. [CrossRef]
44. Wu, Y.H.; He, W.F.; Ma, H.T.; Nie, X.F.; Liang, X.Q.; Pan, J.L.; Wang, S.G.; Shang, M.; Cheng, L. Titanium alloy materials with very high cycle fatigue: A review. *Materials* **2024**, *17*, 2987. [CrossRef] [PubMed]
45. Yoshinaka, F.; Nakamura, T.; Oguma, H.; Fujimura, N.; Takeuchi, A.; Uesugi, M.; Uesugi, K. Characterization of internal fatigue crack initiation in Ti-6Al-4V alloy via synchrotron radiation X-ray computed tomography. *Fatigue Fract. Eng. Mater. Struct.* **2023**, *46*, 2338–2347. [CrossRef]
46. Avateffazeli, M.; Haghshenas, M. Ultrasonic fatigue of laser beam powder bed fused metals: A state-of-the-art review. *Eng. Fail. Anal.* **2022**, *134*, 106015. [CrossRef]
47. Önder, S.; Saklakoglu, N.; Sever, A. Selective laser melting of Ti6Al4V alloy: Effect of post-processing on fatigue life, residual stress, microstructure, microhardness and surface roughness. *Mater. Charact.* **2023**, *196*, 112571. [CrossRef]
48. Karakas, O.; Kardes, F.B.; Foti, P.; Berto, F. An overview of factors affecting high-cycle fatigue of additive manufacturing metals. *Fatigue Fract. Eng. Mater. Struct.* **2023**, *46*, 1649–1668. [CrossRef]
49. Tusher, M.M.H.; Ince, A. Effect of stress-relieved heat treatment on very high cycle fatigue performance of additive manufactured Ti-6Al-4V alloy. *Fatigue Fract. Eng. Mater. Struct.* **2023**, *46*, 3982–4000. [CrossRef]
50. Brot, G.; Koutiri, I.; Bonnand, V.; Favier, V.; Dupuy, C.; Ranc, N.; Aimedieu, P.; Lefebvre, F.; Hauteville, R. Microstructure and defect sensitivities in the very high-cycle fatigue response of laser powder bed fused Ti-6Al-4V. *Int. J. Fatigue* **2023**, *174*, 107710. [CrossRef]
51. Du, L.; Pan, X.; Qian, G.; Zheng, L.; Hong, Y. Crack initiation mechanisms under two stress ratios up to very-high-cycle fatigue regime for a selective laser melted Ti-6Al-4V. *Int. J. Fatigue* **2021**, *149*, 106294. [CrossRef]
52. Pan, X.; Qian, G.; Hong, Y. Nanograin formation in dimple ridges due to local severe-plastic-deformation during ductile fracture. *Scr. Mater.* **2021**, *194*, 11363. [CrossRef]
53. Pan, X.; Xu, S.; Qian, G.; Nikitin, A.; Shanyavskiy, A.; Palin-Luc, T.; Hong, Y. The mechanism of internal fatigue-crack initiation and early growth in a titanium alloy with lamellar and equiaxed microstructure. *Mater. Sci. Eng. A* **2020**, *798*, 140110. [CrossRef]
54. Pan, X.; Su, H.; Liu, X.; Hong, Y. Multi-scale fatigue failure features of titanium alloys with equiaxed or bimodal microstructures from low-cycle to very-high-cycle loading numbers. *Mater. Sci. Eng. A* **2024**, *890*, 145906. [CrossRef]
55. Meyers, M.A.; Chawla, K.K. *Mechanical Behavior of Materials*, 2nd ed.; Cambridge University Press: Cambridge, UK, 2009.
56. Davis, R.F. Hot isostatic pressing. In *Concise Encyclopedia of Advanced Ceramic Materials*; Brook, R.J., Cahn, R.W., Bever, M.B., Eds.; Pergamon: Oxford, UK, 1991; pp. 210–215.
57. Chi, W.; Li, G.; Wang, W.; Sun, C. Interior initiation and early growth of very high cycle fatigue crack in an additively manufactured Ti-alloy. *Int. J. Fatigue* **2022**, *160*, 106862. [CrossRef]
58. Chi, W.; Wang, W.; Li, Y.; Xu, W.; Sun, C. Defect induced cracking and modeling of fatigue strength for an additively manufactured Ti-6Al-4V alloy in very high cycle fatigue regime. *Theor. Appl. Fract. Mech.* **2022**, *119*, 103380. [CrossRef]

59. Fu, R.; Zheng, L.; Zhong, Z.; Hong, Y. High-cycle and very-high-cycle fatigue behavior at two stress ratios of Ti-6Al-4V manufactured via laser powder bed fusion with different surface states. *Fatigue Fract. Eng. Mater. Struct.* **2023**, *46*, 2348–2363. [CrossRef]
60. Hull, D. *Fractography: Observing, Measuring and Interpreting Fracture Surface Topography*; Cambridge University Press: Cambridge, UK, 1999.
61. Fu, R.; Zheng, L.; Ling, C.; Zhong, Z.; Hong, Y. An experimental investigation of fatigue performance and crack initiation characteristics for an SLMed Ti-6Al-4V under different stress ratios up to very-high-cycle regime. *Int. J. Fatigue* **2022**, *164*, 107119. [CrossRef]
62. Sakai, T.; Sato, Y.; Oguma, N. Characteristic S-N properties of high-carbon-chromium-bearing steel under axial loading in long-life fatigue. *Fatigue Fract. Eng. Mater. Struct.* **2002**, *25*, 765–773. [CrossRef]
63. Hong, Y.; Liu, X.; Lei, Z.; Sun, C. The formation mechanism of characteristic region at crack initiation for very-high-cycle fatigue of high-strength steels. *Int. J. Fatigue* **2016**, *89*, 108–118. [CrossRef]
64. Du, L.; Pan, X.; Hong, Y. New insights into microstructure refinement in crack initiation region of very-high-cycle fatigue for SLM Ti-6Al-4V via precession electron diffraction. *Materialia* **2024**, *33*, 102008. [CrossRef]
65. Pan, X.; Su, H.; Sun, C.; Hong, Y. The behavior of crack initiation and early growth in high-cycle and very-high-cycle fatigue regimes for a titanium alloy. *Int. J. Fatigue* **2018**, *115*, 67–78. [CrossRef]
66. Chang, Y.; Zheng, L.; Pan, X.; Hong, Y. Further investigation on microstructure refinement of internal crack initiation region in VHCF regime of high-strength steels. *Frat. Integrità Strutt.* **2019**, *13*, 1–11. [CrossRef]
67. Chang, Y.; Pan, X.; Zheng, L.; Hong, Y. Microstructure refinement and grain size distribution in crack initiation region of very-high-cycle fatigue regime for high-strength alloys. *Int. J. Fatigue* **2020**, *134*, 105473. [CrossRef]
68. Pan, X.; Xu, S.; Nikitin, A.; Shanyavskiy, A.; Palin-Luc, T.; Hong, Y. Crack initiation induced nanograins and facets of a titanium alloy with lamellar and equiaxed microstructure in very-high-cycle fatigue. *Mater. Lett.* **2024**, *357*, 135769. [CrossRef]
69. Piette, T.D.; Warren, R.J.; Spangenberger, A.G.; Hummelt, E.J.; Lados, D.A. Microstructure evolution, fatigue crack growth, and ultrasonic fatigue in as-fabricated laser powder bed and conventionally cast Al-10Si-0.4Mg: A mechanistic understanding and integrated flaw-sensitive fatigue design methods. *Mater. Sci. Eng. A* **2021**, *825*, 141892. [CrossRef]
70. Haigh, B.P. Experiments on the fatigue of brasses. *J. Inst. Metals* **1917**, *18*, 55–86.
71. Goodman, J. *Mechanics Applied to Engineering*; Longmans Green: London, UK, 1899.
72. Gerber, H. *Bestimmung der Zulässigen Spannungen in Eisen-Konstructionen*; Wolf Publishing: Prescott, AZ, USA, 1874; Volume 6, pp. 101–110.
73. Sakai, T.; Sato, Y.; Nagano, Y.; Takeda, M.; Oguma, N. Effect of stress ratio on long life fatigue behavior of high carbon chromium bearing steel under axial loading. *Int. J. Fatigue* **2006**, *28*, 1547–1554. [CrossRef]
74. Pan, X.; Hong, Y. High-cycle and very-high-cycle fatigue behaviour of a titanium alloy with equiaxed microstructure under different mean stresses. *Fatigue Fract. Eng. Mater. Struct.* **2019**, *42*, 1950–1964. [CrossRef]
75. Tao, Z.; Wang, Z.; Pan, X.; Su, T.; Long, X.; Liu, B.; Tang, Q.; Ren, X.; Sun, C.; Qian, G.; et al. A new probabilistic control volume scheme to interpret specimen size effect on fatigue life of additively manufactured titanium alloys. *Int. J. Fatigue* **2024**, *183*, 108262. [CrossRef]
76. Sun, C.; Song, Q.; Zhou, L.; Pan, X. Characteristic of interior crack initiation and early growth for high cycle and very high cycle fatigue of a martensitic stainless steel. *Mater. Sci. Eng. A* **2019**, *758*, 112–120. [CrossRef]
77. Cong, T.; Qian, G.; Zhang, G.; Wu, S.; Pan, X.; Du, L.; Liu, X. Effects of inclusion size and stress ratio on the very-high-cycle fatigue behavior of pearlitic steel. *Int. J. Fatigue* **2021**, *142*, 105958. [CrossRef]
78. Heinz, S.; Balle, F.; Wagner, G.; Eifler, D. Analysis of fatigue properties and failure mechanisms of Ti6Al4V in the very high cycle fatigue regime using ultrasonic technology and 3D laser scanning vibrometry. *Ultrasonics* **2013**, *53*, 1433–1440. [CrossRef]
79. Günther, J.; Krewerth, D.; Lippmann, T.; Leuders, S.; Tröster, T.; Weidner, A.; Biermann, H.; Niendorf, T. Fatigue life of additively manufactured Ti–6Al–4V in the very high cycle fatigue regime. *Int. J. Fatigue* **2017**, *94*, 236–245. [CrossRef]
80. Zenou, M.; Grainger, L. Additive manufacturing of metallic materials. In *Additive Manufacturing: Materials, Processes, Quantifications and Applications*; Zhang, J., Jung, Y.-G., Eds.; Butterworth-Heinemann: Oxford, UK, 2018; pp. 53–103.
81. Zhou, H.; Suzuki, Y.; Kinefuchi, M.; Shibanuma, K. Applicability of the multiscale model for predicting fatigue strength to short and long crack problems. *ISIJ Int.* **2022**, *62*, 2126–2131. [CrossRef]
82. Zhou, H.; Suzuki, Y.; Kinefuchi, M.; Schmauder, S.; Dogahe, K.; Shibanuma, K. Bridging strategy between microscopic and macroscopic crack growth simulations to predict fatigue strength of steels. *Int. J. Fatigue* **2023**, *168*, 107386. [CrossRef]
83. Mlikota, M.; Dogahe, K.; Schmauder, S.; Bozic, Z. Influence of the grain size on the fatigue initiation life curve. *Int. J. Fatigue* **2022**, *158*, 106562. [CrossRef]
84. Yadollahi, A.; Shamsaei, N. Additive manufacturing of fatigue resistant materials: Challenges and opportunities. *Int. J. Fatigue* **2017**, *98*, 14–31. [CrossRef]
85. Yadollahi, A.; Mahtabi, M.; Khalili, A.; Doude, H.; Newman, J. Fatigue life prediction of additively manufactured material: Effects of surface roughness, defect size, and shape. *Fatigue Fract. Eng. Mater. Struct.* **2018**, *41*, 1602–1614. [CrossRef]
86. Ranc, N.; Messager, A.; Junet, A.; Palin-Luc, T.; Buffière, J.Y.; Saintier, N.; Elmay, M.; Mancini, L.; King, A.; Nadot, Y. Internal fatigue crack monitoring during ultrasonic fatigue test using temperature measurements and tomography. *Mech. Mater.* **2022**, *174*, 104471. [CrossRef]

87. Xue, G.G.; Tomoda, Y.; Nakamura, T.; Fujimura, N.; Takahashi, K.; Yoshinaka, F.; Takeuchi, A.; Uesugi, M.; Uesugi, K. Detection of small internal fatigue cracks in Ti-6Al-4V via synchrotron radiation nanocomputed tomography. *Fatigue Fract. Eng. Mater. Struct.* **2022**, *45*, 2693–2702. [CrossRef]
88. Zhan, M.; Wang, X.Y.; Dai, Y.J.; Liu, C.; Chen, Y.; Liu, Y.J.; Wang, C.; Li, L.; Wang, Q.Y.; He, C. The effect of texture on the very high cycle fatigue performance and deformation mechanism of rolled AZ31B magnesium alloys. *Fatigue Fract. Eng. Mater. Struct.* **2024**, *47*, 2521–2536. [CrossRef]
89. Kitagawa, H.; Takahashi, S. Applicability of fracture mechanics to very small cracks or cracks in the early stage. In Proceedings of the Second International Conference on Mechanical Behavior of Materials, ASM, Boston, MA, USA, 16–20 August 1976; pp. 627–631.
90. Cao, F.; Ravi Chandran, K.S. The role of crack origin size and early stage crack growth on high cycle fatigue of powder metallurgy Ti-6Al-4V alloy. *Int. J. Fatigue* **2017**, *102*, 48–58. [CrossRef]
91. Zheng, Y.; Zhao, Z.; Zhang, Z.; Zong, W.; Dong, C. Internal crack initiation characteristics and early growth behaviors for very-high-cycle fatigue of a titanium alloy electron beam welded joints. *Mater. Sci. Eng. A* **2017**, *706*, 311–318. [CrossRef]
92. Pan, X.; Qian, G.; Wu, S.; Fu, Y.; Hong, Y. Internal crack characteristics in very-high-cycle fatigue of a gradient structured titanium alloy. *Sci. Rep.* **2020**, *10*, 4742. [CrossRef]
93. Zhou, H.; Liu, Z.; Kinefuchi, M.; Shibanuma, K. Multiscale modelling strategy for predicting fatigue lives and limits of steels based on a generalised evaluation method of grain boundaries effects. *Int. J. Fatigue* **2022**, *158*, 106749. [CrossRef]
94. Zhou, H.; Liu, Z.; Kikuchi, S.; Shibanuma, K. Analysis of fatigue performance of austenitic stainless steels with bimodal harmonic structures based on multiscale model simulations. *Mater. Des.* **2023**, *226*, 111657. [CrossRef]
95. Hu, Y.; Wu, S.; Wu, Z.; Wu, W.; Qian, W. *Integrity of Additively Manufactured Advanced Mterials and Structures*; National Defense Industry Press: Beijing, China, 2023.
96. Qian, G.; Jian, Z.; Qian, Y.; Pan, X.; Ma, X.; Hong, Y. Very-high-cycle fatigue behavior of AlSi10Mg manufactured by selective laser melting: Effect of build orientation and mean stress. *Int. J. Fatigue* **2020**, *138*, 105696. [CrossRef]
97. Pan, X.; Hong, Y. High-cycle and very-high-cycle fatigue of an additively manufactured aluminium alloy under axial cycling at ultrasonic and conventional frequencies. *Int. J. Fatigue* **2024**, *185*, 108363. [CrossRef]
98. Cheng, Y.T.; Cheng, C.M. Scaling, dimensional analysis, and indentation measurements. *Mat. Sci. Eng. R* **2004**, *44*, 91–149. [CrossRef]
99. Uchic, M.D.; Dimiduk, D.M.; Florando, J.N.; Nix, W.D. Sample dimensions influence strength and crystal plasticity. *Science* **2004**, *305*, 986–989. [CrossRef]
100. Long, X.; Jia, Q.; Li, J.; Chong, K.; Du, L.; Pan, X.; Chang, C. Mechanical properties and parameter optimization of TC4 alloy by additive manufacturing. *China Surf. Eng.* **2022**, *35*, 215–223. (In Chinese)
101. Xu, W.; Lui, E.W.; Pateras, A.; Qian, M.; Brandt, M. In situ tailoring microstructure in additively manufactured Ti-6Al-4V for superior mechanical performance. *Acta Mater.* **2017**, *125*, 390–400. [CrossRef]
102. Chong, Y.; Bhattacharjee, T.; Yi, J.; Shibata, A.; Tsuji, N. Mechanical properties of fully martensite microstructure in Ti-6Al-4V alloy transformed from refined beta grains obtained by rapid heat treatment (RHT). *Scr. Mater.* **2017**, *138*, 66–70. [CrossRef]
103. Qu, Z.; Zhang, Z.; Liu, R.; Xu, L.; Zhang, Y.; Li, X.; Zhao, Z.; Duan, Q.; Wang, S.; Li, S.; et al. High fatigue resistance in a titanium alloy via near-void-free 3D printing. *Nature* **2024**, *626*, 999–1004. [CrossRef] [PubMed]